Micron-size Crystallites of CrO_2 with Insulating Surface Layer

A Thesis

submitted to

Indian Institute of Science Education and Research Pune in partial fulfilment of the requirements for the BS-MS Dual Degree Programme

by

Sumedh Gharwade

Indian Institute of Science Education and Research Pune

Dr. Homi Bhabha Road,

Pashan, Pune 411008, INDIA.

December, 2023

Supervisor: Dr. Ashna Bajpai

Sumedh Gharwade

Certificate

This is to certify that this dissertation "Micron-size Crystallites of CrO_2 with Insulating Surface Layer" towards the partial fulfilment of the BS-MS dual degree programme at the Indian Institute of Science Education and Research, Pune represents study/work carried out by Sumedh Gharwade under the supervision of Dr. Ashna Bajpai, Associate Professor, Department of Physics, during the academic year 2022 – 23.

19-01-24

Dr. Ashna Bajpai

Committee:

Dr. Ashna Bajpai

Dr. Prasenjit Ghosh

I dedicate this thesis to my parents and sister.

Declaration

I hereby declare that the matter embodied in the report entitled Micron-size Crystallites of CrO_2 with Insulating Surface Layer are the results of the work carried out by me at the Department of Physics, Indian Institute of Science Education and Research, Pune, under the supervision of Dr Ashna Bajpai and the same has not been submitted elsewhere for any other degree

Sumedh Gharwade

20/10/2023

Contents

Figures

Tables

Abstract

CrO_2 is a well-known half metallic ferromagnet with T_C ~ 400K. In granular form, surface layer CrO_2 contains another oxide Cr_2O_3, which is an insulator. Due to the presence of insulating surface layer, granular CrO_2 is known to exhibit activated transport, as metallic grains are separated by insulating surface layer, leading to tunneling and consequently a large tunneling magnetoresistance. Here we show that depending on the crystallite size and connectivity, (i) activated transport region along with a metallic region is observed in the electron transport measurement. (ii) In addition to a large tunneling magnetoresistance, significantly large electro resistance has also been observed in these samples. Thus, the electrical transport is not only influenced by ultra-thin surface layer of Cr_2O_3, which is antiferromagnetic and insulating, but also data suggest that the magnetoelectric character of Cr_2O_3 plays a significant role in transport. It is noteworthy that the % MR in 5 Tesla field is similar in magnitude to electro-resistance in few mA of current applied. The influence of magnetoelectric and antiferromagnetic nature of grain boundary is further corroborated by the changes in lattice parameters observed in X-ray diffraction data, which have been analyzed using Rietveld profile refinement. Rietveld Profile Refinement data of X ray diffraction data has been obtained in the temperature range from 300 K to 100 K. This enables us to plot lattice parameters of both CrO_2 and Cr_2O_3 as a function of temperature. These data reveal an anomaly in lattice parameters of Cr_2O_3 in the vicinity of the magnetoelectric transition of Cr_2O_3. These data bring out the role of magnetic state of insulating Cr_2O_3 in electronic transport. The specific heat data in the low temperature region on the granular CrO2 is also been analyzed for obtaining electronic contribution to specific heat.

This thesis extensively examines the mesoscopic and well-defined crystallites of CrO_2, placing a central focus on employing X-ray diffraction (XRD) techniques. The analysis of XRD data utilizes Rietveld refinement, offering in-depth insights into the structural characteristics of the sample. Additionally, this thesis highlights the importance of size and interface effects in granular CrO_2, especially the observation of electro-resistance. This has the potential to propel the development of magnetic tunnel junction technology, with additional tunability.

Acknowledgments

I would like to express my heartfelt gratitude to Dr. Ashna Bajpai, my thesis supervisor, for her unwavering support throughout my master's research project. Her enduring patience and consistent motivation have played a crucial role in guiding me in the right direction. Under her mentorship, I have not only developed essential research skills applicable to both scientific endeavors and broader aspects of life but have also cultivated a research-oriented mindset.

I am also thankful to Dr. Prasenjit Ghosh, my expert advisor for my MS project, for his valuable guidance and encouragement.

My appreciation goes to Dr. Sunil Nair for granting me the opportunity to conduct magneto-transport measurements in his laboratory at the CFMS facility. I am grateful for his generosity in allowing me access to other instruments in the lab. I extend my thanks to Vikram and Rohit from Dr. Sunil Nair's lab for their assistance in magneto-transport measurements on CFMS.

I am deeply grateful to my fellow lab mates, Ajad, Amit, Janani, Shashwat, and Ananth, for their invaluable assistance and support.

I would like to acknowledge the technical support provided by our dedicated team members, including Nilesh Dumbre, Karthikeyan, Anil Prathamshetti, Parveen Nasa, and Sudhir Lone, at various crucial stages throughout my master's project. Additionally, I extend my profound gratitude to the supporting staff at IISER Pune, including the security personnel, housekeeping staff, librarian, and electrician, for their kind and invaluable assistance.

I want to convey my gratitude to my parents and my sister, Leenita, for their unwavering belief in my abilities. I am profoundly thankful for their continuous moral support, boundless love, unwavering encouragement, and, above all, their immense faith in me throughout my journey.

I also take this moment to express my appreciation to my friends - Prabhav, Abhinav, Piyush, Mayank, Vinay, and Bibhut - who have consistently been a significant source of support in my life. Your friendship and encouragement have meant a great deal to me.

This page is intentionally left blank

Chapter 1

Introduction

1.1 A Brief History of CrO_2

Chromium Dioxide (CrO_2), also known as chromium (IV) oxide, is a compound with an interesting history in experimental physics due to its unique magnetic properties and its applications in early magnetic recording technology. In 1956, Norman L. Cox, a chemist working at E.I. DuPont, successfully created acicular chromium dioxide by subjecting chromium trioxide to high temperature (900°F) and pressure in the presence of water. The resulting magnetic crystals took on a slender, glass-like rod shape, making them ideal for use as a magnetic pigment in recording tapes. This breakthrough led to the commercialization of acicular chromium dioxide as a recording medium by DuPont in the late 1960s, under the tradename "Crolyn." In the 1950s, researchers began to investigate the magnetic properties of CrO_2. It was found to be useful for the development of high-density magnetic tapes and disks. This led to the creation of more efficient and compact magnetic recording devices. While CrO_2 was widely used in the 1960s and 1970s in magnetic tapes and floppy disks, it gradually lost its commercial significance due to the development of alternative materials and technologies, such as hard disk drives and solid-state storage devices. level. Despite its decline in commercial applications, research on CrO_2 continued [Ref. 1, 2, 3].

In the late 20th century, with the emergence of spintronics, which focuses on the manipulation of electron spin for data storage and processing, CrO_2 became a subject of interest due to its half metallic character. Researchers explored its potential in spin valve devices and as a magnetic tunnel junction material. The experimental work on CrO_2 was complemented by theoretical studies. Quantum mechanical calculations were used to understand its electronic and magnetic properties at a fundamental It has b also been studied for its potential applications in magnetic sensors, magneto-resistive devices, and as a material for magnetic nanoparticles in various other fields, including biomedical applications. The development of nanotechnology in the late 20th and early 21st centuries opened up new avenues for the manipulation and understanding of CrO_2 at the nanoscale. Researchers explored the properties of CrO_2 nanoparticles and thin films for various applications.

1.2 Crystal Structure

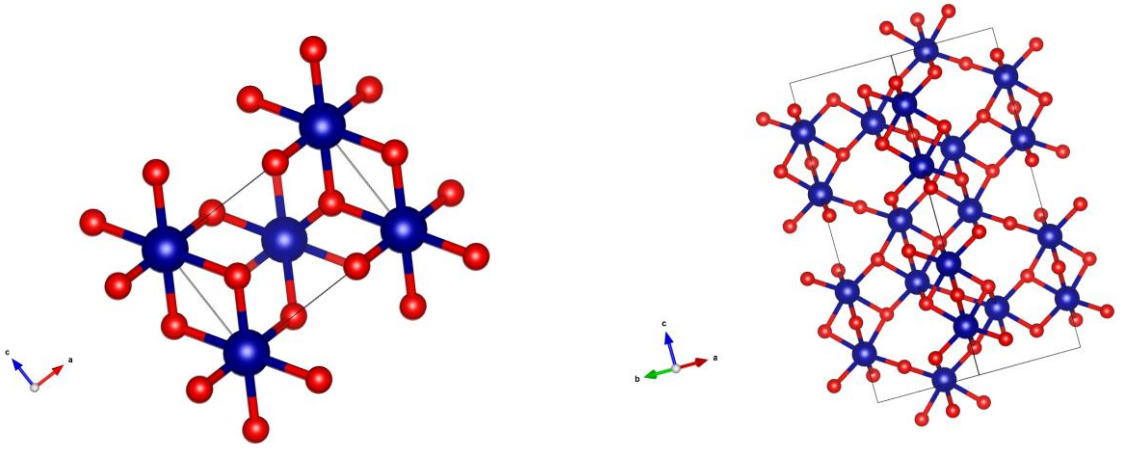

a b

Fig. 1.1 Crystal structures of tetragonal rutile CrO_2 (a) and rhombohedral Cr_2O_3 (b). The blue ball represents chromium atom and the red ones are oxygen. This schematic crystal structure is obtained using vesta software.

CrO_2 exhibits a rutile crystal structure and belongs to the tetragonal $P4_2/mnm$ space group. The cell lattice parameters a, b, c are 4.410 Å, 4.410 Å, 2.910 Å respectively [CrO_2 COD database code: 1516110]. The tetragonal lattice has all of its angles equal to 90°. Within this crystal lattice, each Cr^{4+}(blue) ion is bonded to six equivalent O^{2-}(red) ions, giving rise to a distinctive arrangement of CrO_6 octahedra. These octahedra exist in a combination of corner-sharing and edge-sharing configurations, with corner-sharing octahedral tilt angles measuring 50°, introducing a notable distortion from the ideal octahedral geometry. The compound showcases two distinct Cr–O bond lengths: two of these bonds are shorter, measuring approximately 1.89 Å, while the other four are longer, with lengths of around 1.91 Å. Furthermore, the O^{2-} ions in the structure assume a distorted trigonal planar coordination geometry, being bonded to three equivalent Cr^{4+} ions [Ref. 4].

Cr_2O_3 a corundum crystal structure within the $R\bar{3}c$ space group. The cell lattice parameters a, b, c are 4.9607 Å, 4.9607 Å, 13.599 Å respectively [Cr_2O_3 COD database code: 9008084]. Lattice angles α, β, ɣ are 90º, 90º, 120º respectively. The central chromium ions Cr^{3+} (blue) exhibit intricate bonds with six equivalent oxygen ions O^{2-}(red), forming corner-sharing, face-sharing, and edge-sharing CrO_6 octahedra [Ref. 5]. The corner-sharing octahedral tilt angles span a range from 47 to 60 degrees, indicating a degree of distortion from ideal octahedral symmetry. This distortion gives rise to three shorter Cr–O bond lengths, each measuring approximately 1.97 Å, as well as three longer bonds at around 2.02 Å. Additionally, the oxygen

ions (O^{2-}) are bonded to four equivalent Cr^{3+} atoms, shaping a mixture of distorted corner and edge-sharing OCr_4 trigonal pyramids [Ref. 5].

1.3 Exchange interactions:

Exchange interactions stem from electrostatic forces, as similar charges incur energy costs when close but save energy when apart. When two electrons in an atom exhibit antiparallel spins, they can share the same atomic or molecular orbital. However, this setup amplifies Coulombic repulsion between electrons. Consequently, it is energetically advantageous for electrons to possess parallel spins and, adhering to Pauli's exclusion principle, occupy distinct orbitals. These interactions, crucial for establishing long-range magnetic order, come in various types hinging on the distance and arrangement of magnetic ions. Expressing energy through the dot product of spins and the magnetic field, we can encapsulate these interactions in a Hamiltonian:

$$\hat{\mathcal{H}} = -\sum_{ij} J_{ij} \mathbf{S}_i \cdot \mathbf{S}_j$$

In this equation, J_{ij} signifies the exchange constant between the i^{th} and j^{th} spins, denoted as S

1.3.1 Direct Exchange Interaction:

In cases of direct exchange, electrons on adjacent magnetic atoms engage in exchange interactions without requiring the involvement of an intermediary atom.

1.3.2 Double Exchange Interaction:

This form of interaction is possible in oxides, particularly when magnetic ions at distinct lattice sites exhibit varying valencies. There is also indirect exchange with two magnetic ions separated by a nonmagnetic one. This leads to a ferromagnetic ordering observed in CrO_2 [Ref. 7, 8, 9].

1.3.3 Superexchange Interaction:

This form of interaction operates between two magnetic ions that are not adjacent, facilitated by a non-magnetic intermediary ion. This leads to antiferromagnetic ordering observed in Cr_2O_3 [Ref. 10]

1.4 Electric and Magnetic Properties

1.4.1 Paramagnetism:

Paramagnetic materials have atoms or molecules with unpaired electrons in their electron configuration. These unpaired electrons give rise to magnetic moments. When placed in a strong external magnetic field, the magnetic moments of the unpaired electrons align themselves with the field, causing the material to be weakly attracted to the field. The strength of paramagnetism decreases as temperature increases. This is because at higher temperatures, the thermal energy disrupts the alignment of the atomic or molecular magnetic moments. The random thermal motion of particles counteracts the alignment caused by the external magnetic field. In some cases, such as certain metallic elements like sodium and other alkali metals, the paramagnetism is relatively weak and remains nearly independent of temperature. This is because the unpaired electrons in the conduction band are responsible for the paramagnetic behaviour, and their motion is relatively unaffected by temperature [Ref. 6].

1.4.2 Ferromagnetism:

Ferromagnetic materials display a phenomenon of long-range atomic-level ordering, resulting in the alignment of unpaired electron spins within specific regions known as domains. In these domains, the magnetic field is notably strong. However, in a bulk sample of the material, it typically remains demagnetized because the domains are randomly oriented in relation to each other. This distinctive behaviour of ferromagnetism becomes evident when a minor external magnetic field, such as one generated by a solenoid, induces the alignment of magnetic domains within the material, rendering it magnetized. This external magnetic field is then significantly amplified, often expressed as the material's relative permeability. Ferromagnetic materials tend to retain some degree of magnetization even after the external magnetic field is removed, which is referred to as remanence. The fraction of the saturation magnetization retained when the driving field is discontinued is termed the remanence of the material and holds significant importance in the context of permanent magnets. Ferromagnetic materials possess a maximum temperature, known as the Curie Temperature, beyond which their ferromagnetic properties vanish due to the effects of thermal agitation. In CrO_2, the localization of the d_{xy} orbital (due to the distortion of the CrO_6 octahedral symmetry) and the involvement

of two different types of orbitals in the electron hopping process (using double exchange interaction) are crucial for the ferromagnetic behaviour of CrO_2 [Ref. 6, 7, 8, 9].

1.4.3 Anti ferromagnetism:

Anti ferromagnetism is a magnetic behaviour where the neighbouring ions, acting as miniature magnets, spontaneously arrange themselves into opposing, or antiparallel, configurations. In antiferromagnetic materials, the magnetic alignment of atoms or ions in one direction is effectively cancelled out by those aligned in the opposite direction since the exchange constant $J_{j,k}$ is negative below certain temperature This natural antiparallel arrangement of atomic magnets is disrupted as the material is heated and completely disappears above a specific temperature known as the Néel temperature, which is unique to each antiferromagnetic substance. In Cr_2O_3 indirect exchange interaction leads to antiferromagnetic ordering below 307K [Ref. 6, 10].

1.4.4 Linear magnetoelectric effect:

The linear magnetoelectric (ME) effect is the linear response of the magnetization of a material to an applied electric field, or the corresponding electric polarization induced by a magnetic field,

$$\mu_0 M_i = \alpha_{ij} E_j$$

$$P_i = \alpha_{ij} H_j$$

where α_{ij} denotes the magnetoelectric tensor.

Notably, this phenomenon is observable solely in materials where both space-inversion and time-reversal symmetries are broken. Cr_2O_3 is a notable example of a material exhibiting this intriguing magnetoelectric effect [Ref. 12].

1.4.5 Metallic behaviour:

The electronic band structure of CrO_2 have bands primarily composed of oxygen 2p character crossing the Fermi level. These bands are distinct from the typical p states that arise from d-p hybridization seen in other transition metal oxides. The presence of almost pure p states near the Fermi level acts as electron or hole reservoirs, causing a nonintegral occupation of the d bands. This effect is termed "self-doping". The self-doping effect plays a crucial role in the ability of CrO_2 to exhibit metallic behavior since it allows the material to behave as a metal even in the presence of relatively large values of the Hubbard U parameter, which usually leads to insulating behavior in other materials (Mott insulators). Here the d band is split into two parts. One is below the Fermi level, leading to localized spin and second is itinerant d band hybridized with p band. That reduces the effect of on-site d-d Coulomb interaction and hence CrO_2 is a ferromagnetic metal, rather than antiferromagnetic insulator. We clearly observe metallic behavior in thin films of CrO_2 grown on substrates like TiO_2 [Ref. 9, 11].

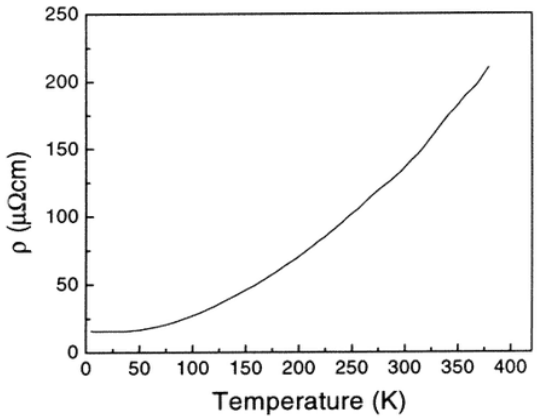

Fig 1.2 Transport measurement on CrO_2 thin film [Ref. 11]

1.4.6 Half metallic behaviour:

A half metal has an electronic structure that is unusual in the sense that it exhibits different behaviours for electrons with different spin states. For one spin direction (usually the majority spin), it behaves like a metal, with a Fermi surface. However, for the opposite spin direction (usually the minority spin), there's a gap in the spin-polarized density of states, making it similar to a semiconductor or insulator. One of the distinctive features of half metals is their differential response to external fields. They typically have electric conductivity because one spin direction behaves like a metal, allowing for charge transport. However, they exhibit no high-field magnetic susceptibility, which means their magnetization doesn't respond strongly to magnetic fields, particularly at low temperatures. This is because one of the spin directions already has a gap in the density of states, and the available states are fully occupied. Many

metal Oxides including CrO_2 are Type 1 Half metal, having less than 5 d electrons. In such compounds unpolarized 4 s states are shifted above fermi level level due to hybridization with 2p oxygen states.

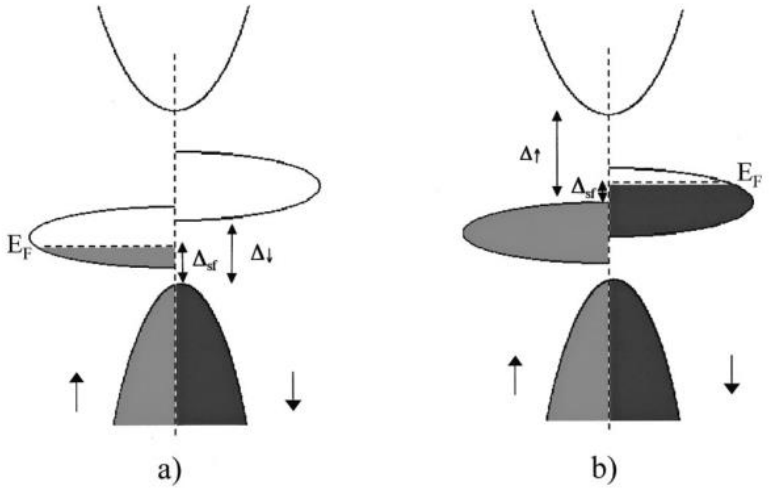

Fig 1.3 Schematic density of states for half metal, (a)Type Ia and (b)Type II [Ref. 13].

1.4.7 Spin Polarization:

It's a measure of alignment of spin in a particular direction

$$P = \frac{N_\uparrow - N_\downarrow}{N_\uparrow + N_\downarrow}$$

where $(N_\uparrow, N_\downarrow)$ represent the densities of states for electrons with spin "up" and "down" orientations at the Fermi level, respectively.

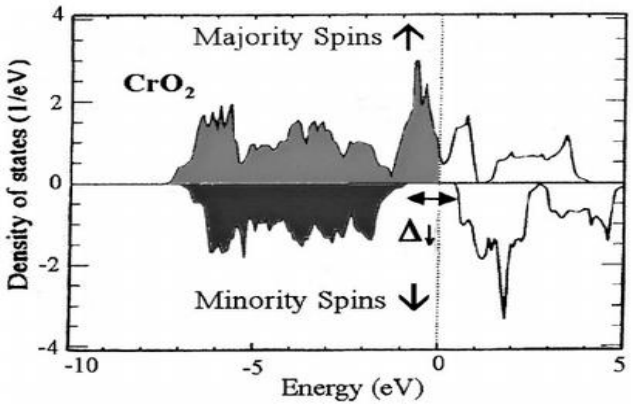

Fig 1.4 Spin polarization in of CrO_2 [Ref. 13].

1.4.8 Magnetoresistance:

The variation of resistance in presence of magnetic field is known as magnetoresistance.

$$\Delta R(B) = \frac{R(B) - R(0)}{R(0)}$$

Its functional form depends on multiple factors. Here we show resistance as a function of Temperature for granular CrO_2. Here the sample consists of micron size crystallites of CrO_2, containing a surface layer of insulating Cr_2O_3. This leads to resistance decreasing with temperature and hence activated transport, instead of metallic behaviour expected from CrO_2 phase.

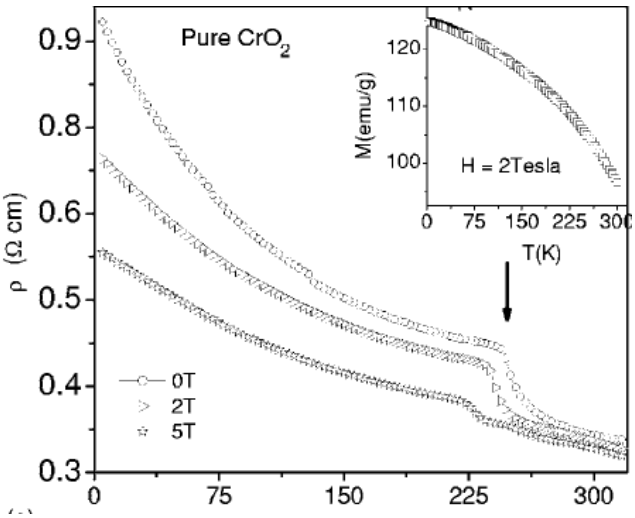

Fig 1.5 CrO_2 magneto-transport [Ref. 17]

The magneto-transport measurements were done on the pressed pellet of granular CrO_2. These samples are synthesized using a synthesis technique, which does not need pressure as a control parameter [ref. 35]. It is noteworthy that CrO_2 is not known to form in ambient pressure. In addition, this compound is metastable in nature, which means it even more difficult to stabilize pure CrO_2 phase. Commercially available CrO_2, synthesized using high pressure synthesis technique form, in needle shaped grains, which are 100-400 nm long. However, the CrO_2 samples discussed in this thesis are micron size grains. In the following section, we discuss key differences between CrO_2 samples presented in this thesis vis a vis commercially available CrO_2.

1.5 Comparison of commercially available CrO_2 with micron sized sample:

(Micron sized samples were synthesized using technique described in ref 35)

- At 5 K, commercial powders exhibit a magnetic saturation (M_s) within the range of 100–110 emu/g, while our sample demonstrates a higher M_s of 127–135 emu/g under the same conditions, which is close to theoretically predicted value. Similarly, at 300 K, commercial powders show an M_s of 80 emu/g, whereas our sample presents a heightened value ranging from 100 to 110 emu/g [Ref 35].
- The coercivity (H_c) of commercial powders stands at 1 kOe at 5 K, contrasting with our samples indicating a lower H_c of 50 Oe. At 300 K, commercial powders have an H_c of 600 Oe, while our samples show decreased H_c of 10 Oe [Ref 35].
- Remanence (MR) values also differ, with commercial powders ranging from 75 to 80 emu/g, while our sample shows a reduced MR of 10–20 emu/g [Ref 35].
- In terms of grain characteristics, commercial powders typically feature a grain size of 0.1–0.4 μm, whereas our sample shows a broader range of 1–10 μm. Additionally, the grain shape and aspect ratio vary; commercial powders have needle-shaped grains with an aspect ratio of 9:1, whereas our sample contain rod-shaped grains with a variable aspect ratio [Ref 35].
- Magnetoresistance in the pressed pellet (containing micron-size rods of CrO_2) is observed to increase by approximately 25% at 230 K [Ref 17], whereas in commercial powders, it is noted to be less than 1% around room temperature.

In the upcoming chapter, we delve into various methods and tools employed to comprehend the morphology, structure, and transport properties of our sample (Chapter 2). Moving forward, Chapter 3 provides a thorough examination of sample morphology through SEM, while also exploring its structure through XRD and Rietveld Refinement. Additionally, we explore the temperature-induced transformations in cell parameters. The following chapter, Chapter 4, delves into the measurement of specific heat data for our sample. Chapter 5 focuses on transport measurements conducted using Linkam, CCR and CFMS setups. Finally, Chapter 6 wraps up the thesis with conclusions and outlines future prospects.

Chapter 2

Characterization techniques and instruments

2.1 Scanning Electron Microscope:

When a high-energy electron beam is directed onto a sample, it causes the emission of secondary electrons with relatively low energy. These secondary electrons provide information about the sample's topography. Some of the incident electron beam is scattered backward by the atomic electron cloud of the sample, resulting in what is known as backscattered electrons (BSE). The scattering cross-section of these BSE is influenced by the atomic density of the sample. Samples with higher atomic density produce more BSE, resulting in a brighter image with improved contrast resolution. Additionally, when secondary electrons are emitted from the inner electron shells of atoms, the outer shell electrons fill the emptied inner shells, leading to the emission of characteristic x-ray photons with energy levels corresponding to the energy difference. The wavelengths of these emitted x-ray photons are unique to the atom, allowing for the determination of the sample's elemental composition.

A typical SEM setup involves directing a focused beam of high-energy electrons at the sample's surface, where it interacts with the sample's atoms. Detectors collect the emitted electrons to create an image and provide information about the sample's composition. The electron beam is manipulated by scanning coils and deflector plates, resulting in a raster scan of the sample's surface. Detectors and amplifiers process the emitted electrons' intensity distribution to generate an image. It's important for the sample to be conductive, allowing the beam to scan its surface for conventional imaging. Non-conductive samples can be coated with a conducting material using techniques like sputter coating or high vacuum evaporation [Ref. 37, 38].

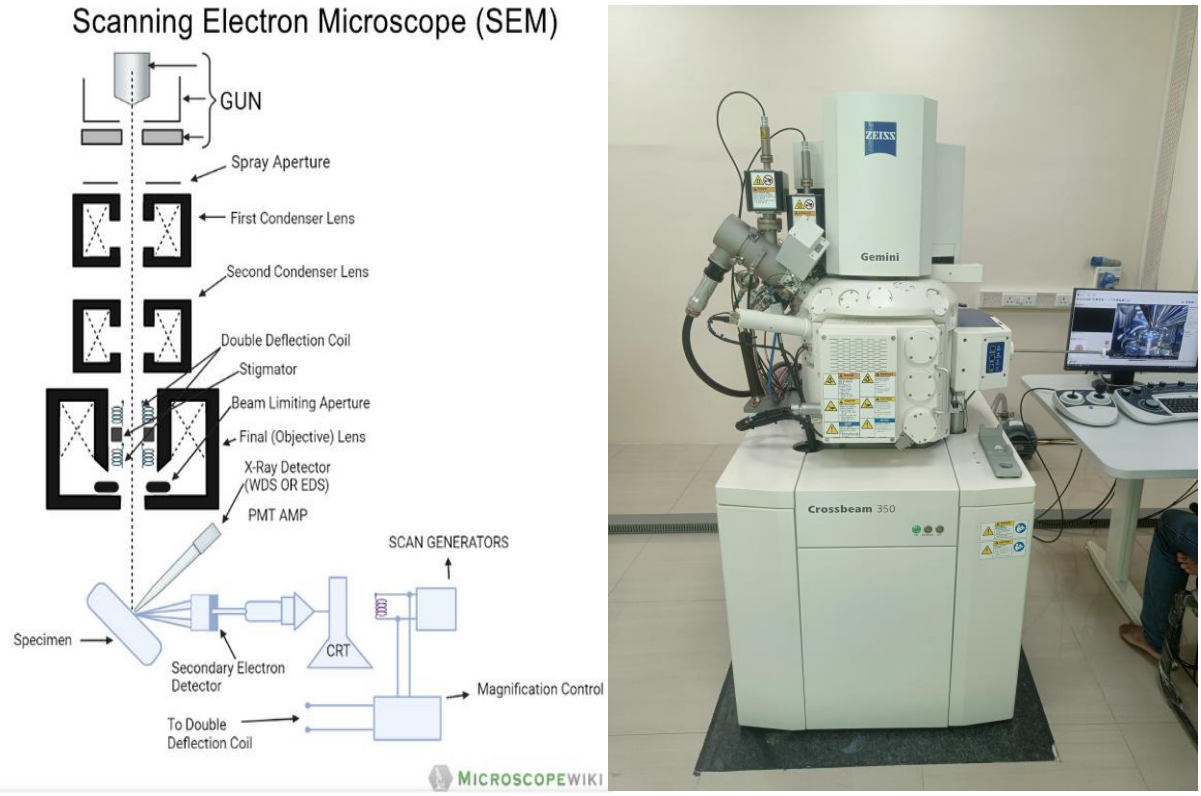

A B

Fig 2.1 A) Schematic diagram of SEM [Ref. 34] and B) FESEM setup

2.2 X-ray Diffraction:

X-ray powder diffraction is a rapid analytical technique used to determine information of crystalline material such as phases, cell dimension, atomic spacing etc

Crystalline materials comprise of regular array of atoms. Monochromatic X-rays get scattered due to such atomic arrays of the target material which produce constructive and destructive interference obeyed by Bragg's law.

$$n\lambda = 2d \sin\theta$$

Where,

- d is lattice spacing,
- θ is incident angle
- λ is wavelength
- n is any integer

The X rays diffracted from the sample are collected at the detector. XRD pattern intensities provide information about the arrangement of atoms in the crystal structure. Polycrystalline samples contain tiny crystallites oriented in all possible directions. When such a sample is exposed to the X-ray beam, the XRD pattern will contain all possible planes and hence the sample scanning is done through a range of 2θ angles.

The diffraction patterns were recorded in the Bragg-Brentano geometry. This geometry offers the advantages of high resolution and high beam intensity analysis at the cost of very carefully prepared samples. To identify various phases, present in sample, recorded data was compared with data available on AMCS and COD [Ref. 39, 40].

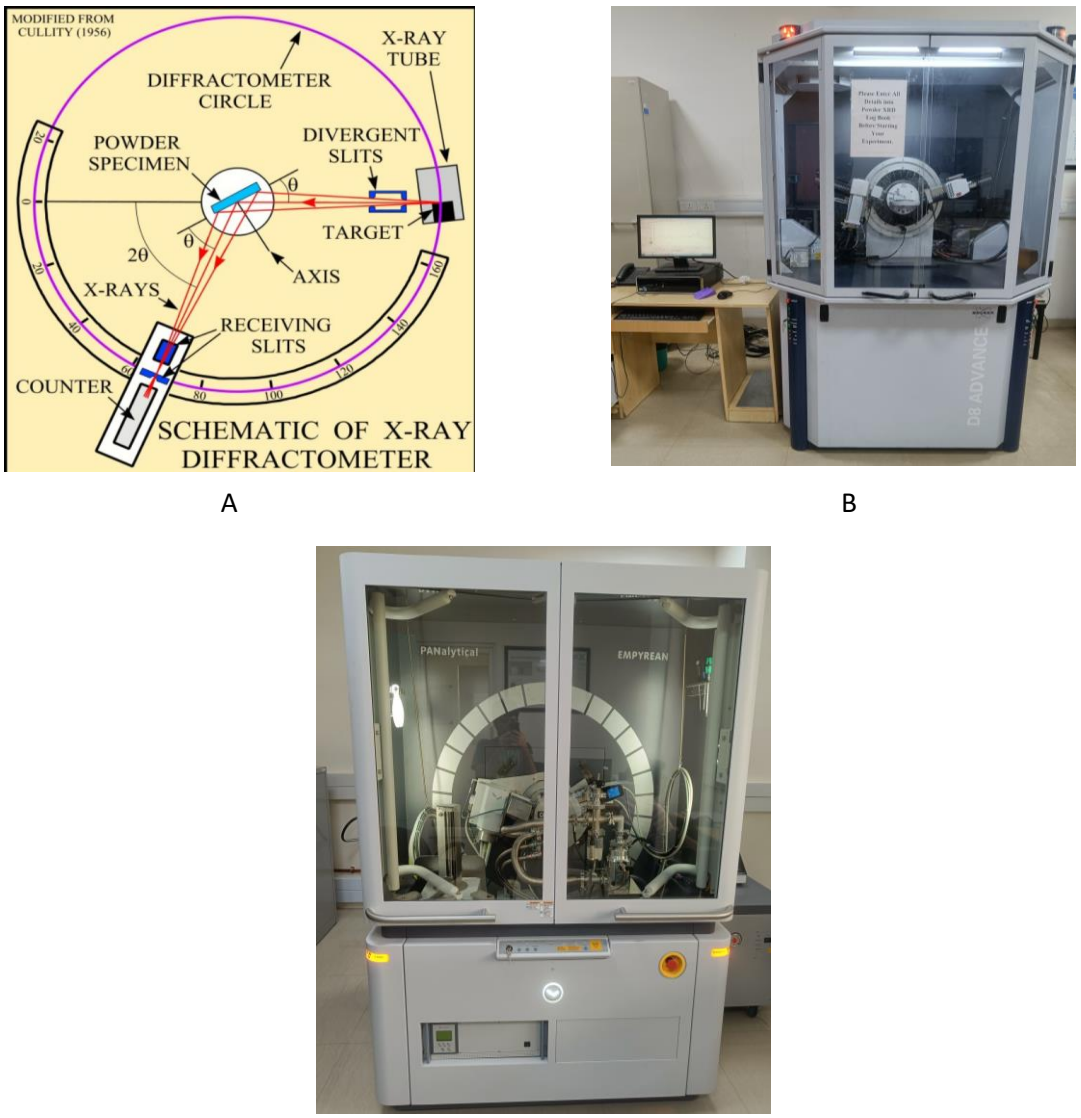

A B

C

Fig 2.2 (A) Schematic diagram of X ray diffractometer [Ref. 36], (B)Bruker D8 advance and (C) PANalytical Instrument.

2.3 Rietveld Refinement:

Rietveld refinement is a technique devised by Hugo Rietveld for crystalline materials. The Rietveld method refines user-selected parameters to minimize the difference between data observed and a hypothesized/theoretical crystal model. The observed diffraction pattern is refined using least square method.

In XRD pattern intensities y_i are recorded at various incremental steps i (angles). The quantity to be minimized is the residual function S_y given by:

$$S_y = \sum_i w_i (y_i - y_{ci})^2$$

where, $w_i = 1/y_i$,

y_i = observed intensity at the ith step,

y_{ci} = calculated intensity at the ith step.

A typical powder diffraction pattern comprises multiple reflections, each characterized by peak height, peak width, peak position, and an integrated area, all of which are related to the Bragg intensity I_K. In this context, K denotes the Miller indices (h, k, l), and I_K is directly related to the square of the absolute value of the structure factor F_K. Generally, the observed intensity y_i results from contributions of various Bragg reflections. The calculated intensity y_{ci} is determined based on $|F_K|^2$ derived from the structural model. The formula for calculating y_{ci} is as follows:

$$y_{ci} = s \sum_K L_K \, |F_K|^2 \varphi(2\vartheta_I - 2\vartheta_K) \, P_K A + y_{bi}$$

where,

- "s" denotes the scale factor.
- "K" represents the Miller indices (h, k, l), for a particular Bragg reflection.
- "L_K" stands for the Lorentz-Polarization factor.
- "F_K" refers to the structure factor associated with the Kth Bragg reflection.
- "φ" represents the reflection profile function.
- "P_K" signifies the preferred orientation factor.
- "A" represents the volume absorption factor.

y_{bi} is the background intensity at the ist step. The background intensity value, denoted as y_{bi} at the ist step, can be determined through various methods. These methods include:

1. User-Supplied File: Users can provide a file containing background intensity values.
2. Linear Interpolation**:** The background intensity can be obtained by linearly interpolating between user-selected points.
3. Specific Background Function: A specific background function is used to calculate the background intensity. This function is typically a fifth-order polynomial function. Alternatively, users can provide a custom background function in the form of a user-generated .BGR file, which may have refinable parameters for background heights.

The reflection profile function, denoted as φ, is responsible for approximating the effects of both instrumental features and sample features.

In the data presented in this thesis, a pseudo-Voigt function was employed for refining. The width parameter "H" in the reflection profile is modeled using Caglioti's formula, which is expressed as:

$$H^2 = U \tan^2\theta + V \tan\theta + W$$

The parameters U, V, and W in the formula are adjustable parameters used to fine-tune the width and shape of the reflection profile during data refinement.

In the default calculation model, it is assumed that there is an equal number of crystallites contributing to each diffraction peak. However, these crystallites are randomly oriented, and there may be a preference or tendency for them to align in a specific way. This preferred orientation can lead to distortions in the peak intensities. To correct for these distortions, a March distribution function is employed.

$$P_K = [G_1 \cos^2(\alpha K) + G_1^{-1} \sin^2(\alpha K)]^{-3/2}$$

This function is used to correct for the effects of preferred orientation, ensuring that the analysis accounts for the real distribution of crystallite orientations.

The structure factor F_K is given by:

$$|F_K|^2 = m_K \left| \sum_{n=1}^{N} f_n \, e^{-B_n \frac{sin\theta}{\lambda^2}} \, e^{2\pi i \, (hx_n + ky_n + lz_n)} \right|^2$$

Where,

- "N" represents the total number of atoms.
- "(x_n, y_n, z_n)" are the coordinates specifying the position of the nth atom.
- "f_n" corresponds to the atomic structure factor.
- "B_n" refers to the Debye-Waller factor, which is also known as the temperature factor. This factor is used to account for the thermal vibrations and displacements of atoms within the material.

The Lorentz-Polarization factor L_K takes into account instrumental factors, specifically the polarization of the X-ray beam due to the scattering of light from the atom and the diffraction from the monochromator. These factors are included to address the polarization effects that can occur during the X-ray diffraction experiment [Ref. 41].

2.4 Linkam stage:

Linkam stage is used for electrical transport measurement, where four metallic probes are available to make connections. Using Liquid N2 flow in the Linkam stage, we reach -120 degree Celsius. Linkam stages can be equipped with electrical connections or gold-tipped tungsten needle probes, enabling measurement of a sample's electrical properties and their temperature-dependent variations. Linkam systems can integrate with various optical and spectroscopic techniques, such as Raman. For electrical measurement, the design of Linkam stage is more suitable for probing resistance of thin film samples or devices, which are larger in area. For cold pressed pellets of the size few mm^2, it requires lot of care so that metallic probes in the form of sharp needles do not short with each other during the course of measurement [Ref. 42].

Fig 2.3 Linkam setup

2.5 Physical Property Measurement System:

The PPMS is a computerized system designed for conducting measurements on materials at low temperatures and in the presence of a magnetic field. It allows for the assessment of various material properties, such as specific heat, magnetic susceptibility in both alternating and direct current, as well as electrical and thermal transport characteristics, including the Hall Effect, thermoelectric figure of merit, and the Seebeck-Effect [Ref. 43].

A

B

Fig 2.4 (A) PPMS setup and (B) PPMS probe

2.6 Closed Cycle Refrigerator:

Closed cycle refrigerators (CCRs) are electrical machines designed for cooling purposes, utilizing the Gifford-McMahon cooling cycle. The refrigeration process begins by turning the valve disk, which in turn opens the high-pressure pathway. This allows high-pressure helium gas to flow through a regenerating material and enter the expansion space, starting the cooling process. Instead of employing a mechanical piston, a pressure difference is used to move the displacer. This pressure difference pushes the displacer "up," causing the gas at the bottom of the system to expand and cool. The rotation of the valve disk also opens the low-pressure pathway, enabling the now colder, lower-pressure gas to pass through the regenerating material and absorb heat from the system, further enhancing the cooling effect. Once the pressure difference is established, the displacer returns to its original position, completing the cycle [Ref. 44].

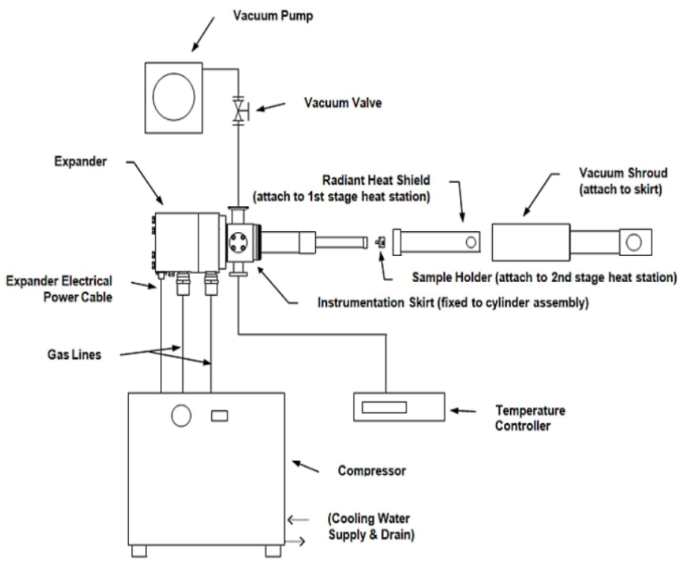

Fig 2.5 Schematic diagram of CCR setup

2.7 Cryogen Free Measurement Systems:

The system consists of a pulse tube cryocooler, a cryostat equipped with a superconducting magnet (upto 7 Tesla), an adjustable temperature sample area, a range of specialized probes for diverse physical property measurements, along with electronic components, computer interfaces, and measurement software. Both the magnet and the sample space are cooled using the cryocooler. High resolution 20-bit power supplies Ensures precise and stable magnet operation [Ref. 45].

Fig 2.6 CFMS facility for Magneto-transport measurement

Chapter 3

SEM, XRD and Rietveld Refinement

In this chapter we present preliminary characterization of the CrO_2 samples using SEM, XRD and temperature variation of XRD. We also present Rietveld profile refinement of XRD data. A number of CrO_2 samples were investigated in powder as well as pellet form. Pellets were further classified into two categories. In first case as-prepared powders were cold-pressed into the form of a pellet. It is known in literature that cold pressed pellets of granular CrO_2 is susceptible to generating micro-cracks which makes transport measurements difficult. Unlike other oxides, it is difficult to sinter CrO_2 pellet at high temperatures as it is a metastable compound. While commercially available CrO_2 powders or of needle shape are reported in cold -pressed form, we present data on cold -pressed pellets of micron-size crystallites. In the second case, the precursor was pelletized during synthesis procedure and hence the CrO_2 were formed in the pellet form, with its granular structure intact. This leads to soft pellets, however it is easy to do transport measurements in such as-prepared pellets. The details of the synthesis procedure can be found in reference 35.

3.1 SEM Observation

We successfully observed micron-sized crystals of chromium dioxide (CrO_2) using scanning electron microscopy (SEM). Furthermore, we observed that when the sintered samples were crushed and cold-pressed, it led to the fracturing of individual grains within the material.

Table 3.1 Features of CrO_2 grains

Sample name	Code	Form	Shape
A1	Cr 27 Dry	Powder	Micron sized hexagonal and octagonal CrO_2 rods
A2	Cr 41 Dry	Pellet	Sample consists of both thick and thin-rods of CrO_2
A3a	Cr 43 Dry	Pellet	Micron sized CrO_2 rectangular rods
A3b	Cr 43 Dry	Cold pressed pellet	Irregular shaped fractured small CrO_2 grains
A4	R2	Pellet	Cuboid shaped CrO_2 grains

3.1.1 A1:

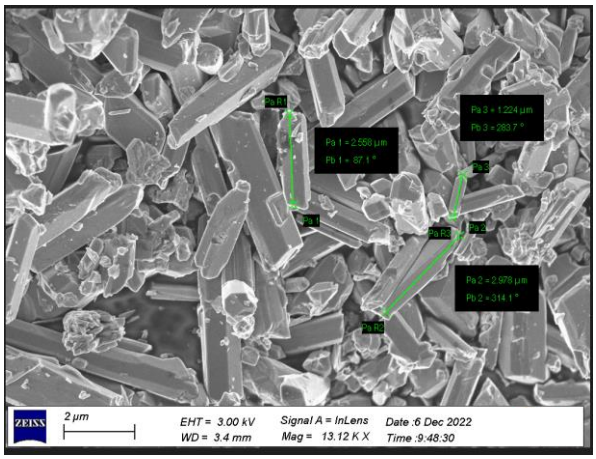

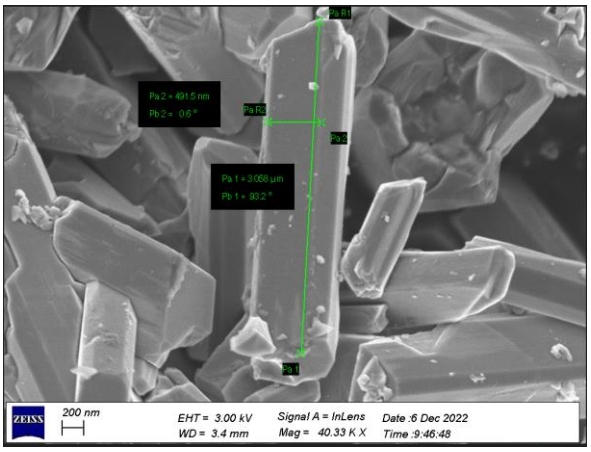

3.1.2 A2:

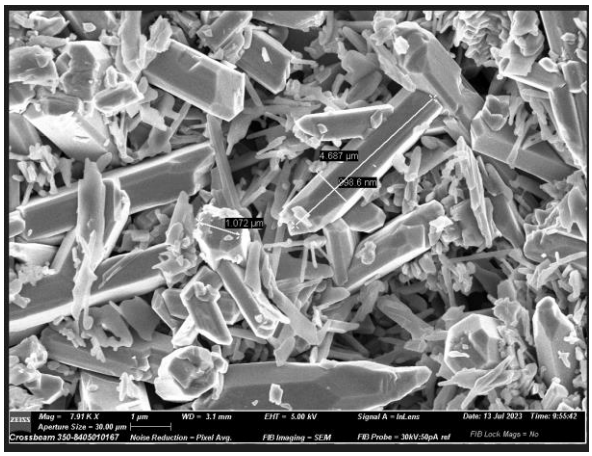

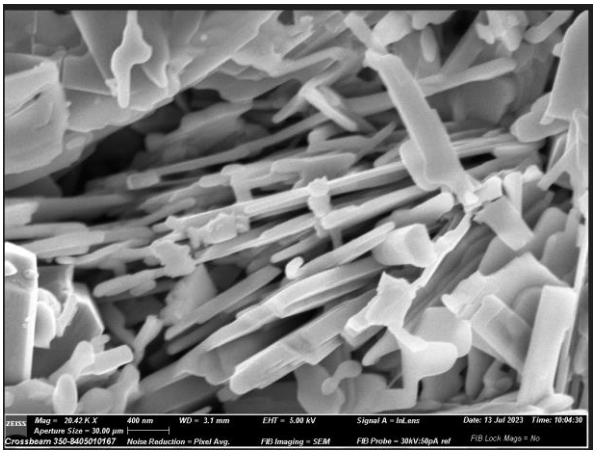

3.1.3 A3a:

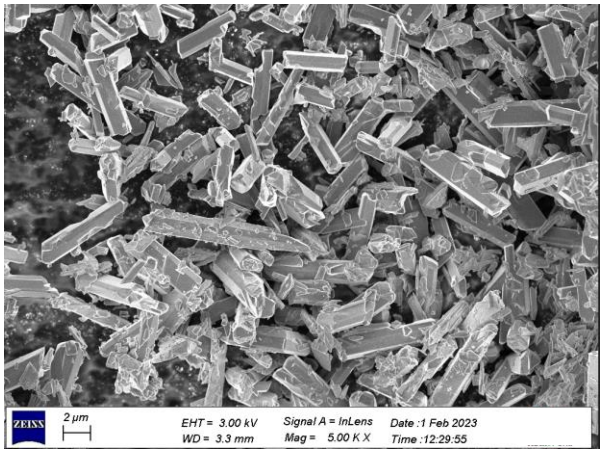

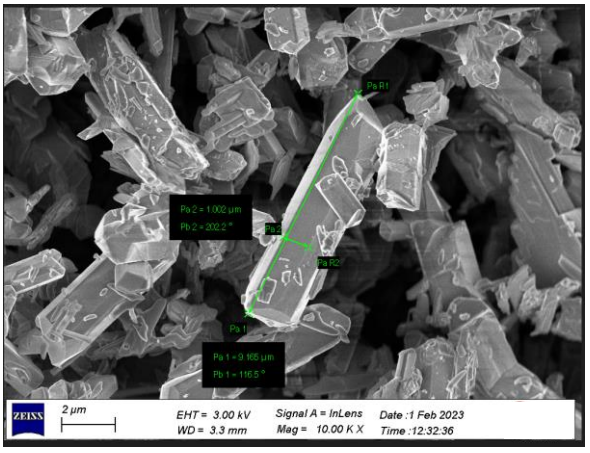

3.1.4 A3b:

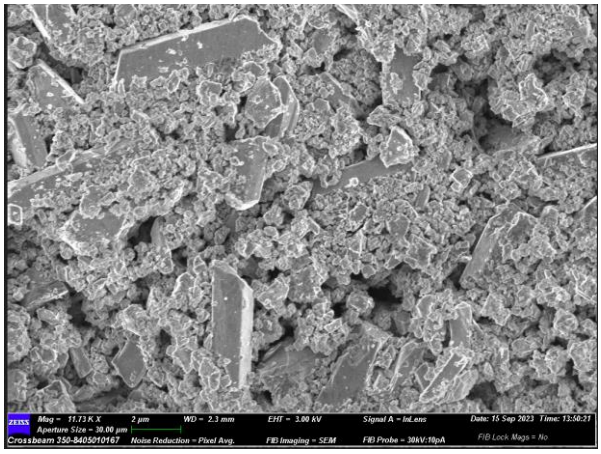

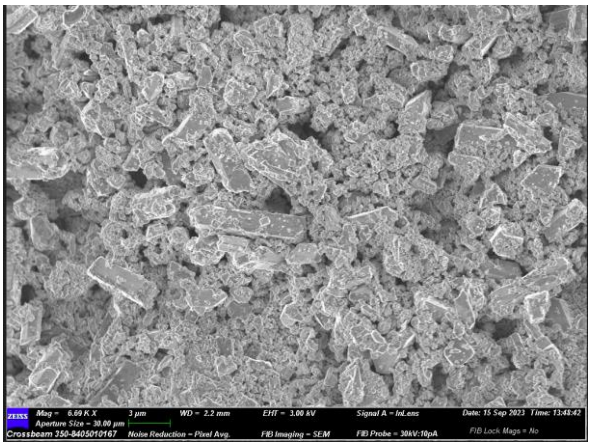

3.1.5 A4:

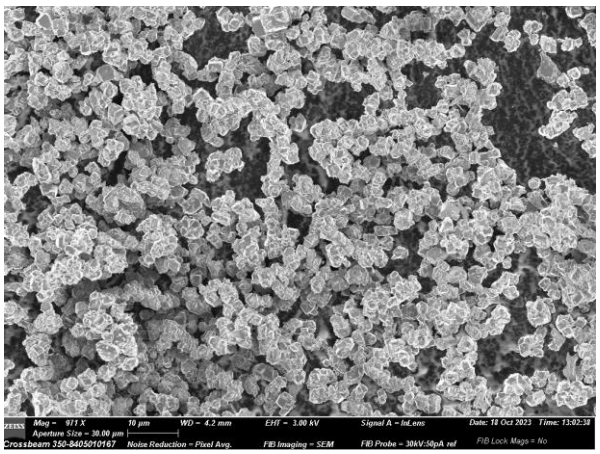

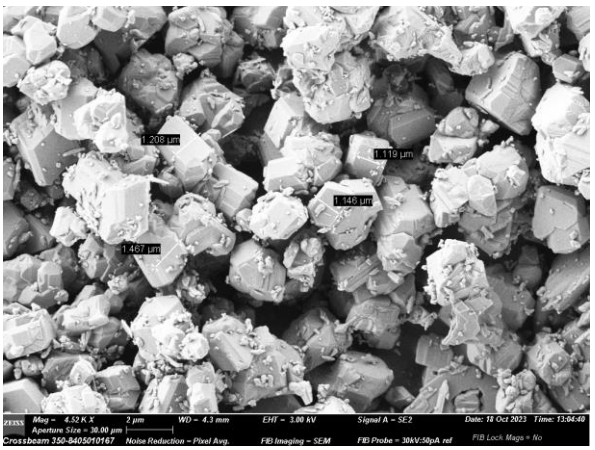

3.2 Procedure for Rietveld Refinement of XRD data:

A brief fitting procedure is listed below.

1. Scale factor.
2. Scale factor, zero point of detector, background parameter and instrumental parameters. The background was fixed using linear interpolation with a set of pre-decided points provided by user.
3. Refine the lattice parameters
4. Refine full width half maximum/shape parameters
5. Refine atomic positions
6. Add preferred orientation.
7. Add the overall Debye-Waller factors.

3.3 Room Temperature XRD:

In this section, we present Rietveld profile refinement of lab XRD data at room temperature on two samples (A1 and A3). The measurements were done on the Bruker d8 setup (G1, IISER Pune). The sample, in powder form, was evenly distributed on a glass cover slip positioned within the sample holder space of the XRD setup. The CrO_2 phase possesses a $P4_2/mnm$ structure, and its standard cell lattice parameters, represented by the lengths a, b, and c, are 4.410 Å, 4.410 Å, and 2.910 Å, respectively [Ref. 4, CrO_2 COD database code: 1516110].

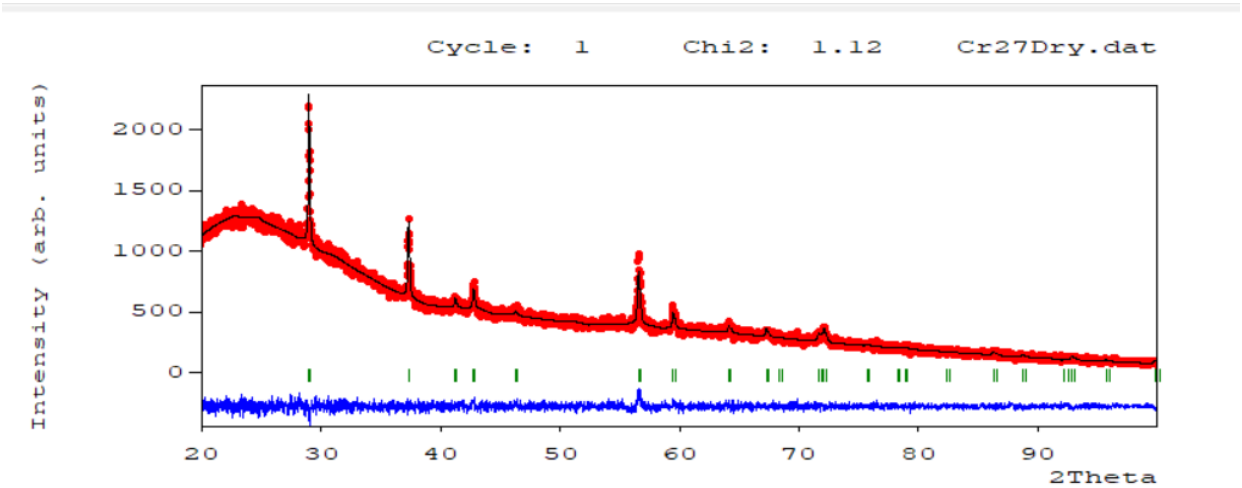

Fig 3.1 XRD and Rietveld Refinement for sample A1

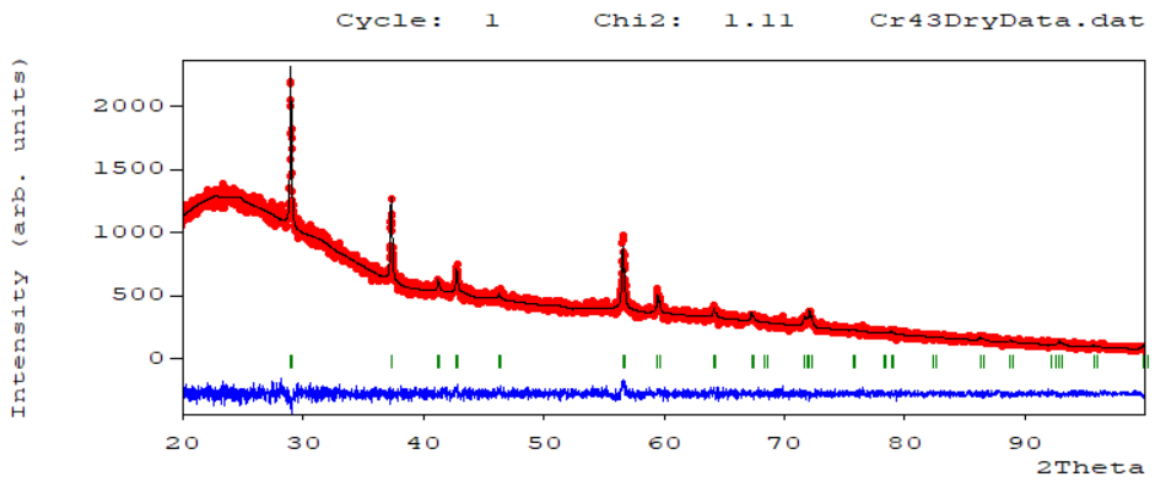

Fig 3.2 XRD and Rietveld Refinement for sample A3a

Figures 3.1 and 3.2 show the results of Rietveld refinement. Here the red dots are experimentally observed data and the black line is the fitted data. The green vertical lines represent Bragg peak corresponding to CIF files obtained from COD database [COD database code 1516110]. The blue line represents the difference. It is noteworthy that Cr_2O_3 phase, which appears as an ultra -thin surface layer of 2-3 nm [Ref 20] is not picked in lab XRD mostly due to glass background noise. Hence, very good χ^2 value was achieved for the samples.

3.4 Low Temperature XRD:

In this section, we present Rietveld profile refinement done on Panalytical Empyrean instrument setup (Chemistry wing, Main Building, IISER Pune) for sample A1. We performed low temperature XRD in the temperature range of 300 to 50 K. The sample, in powder form, was evenly distributed on a quartz glass cover slip positioned within the sample holder space of the XRD setup. The CrO_2 phase possesses a $P4_2/mnm$ structure, and its standard cell lattice parameters, represented by the lengths a, b, and c, are 4.410 Å, 4.410 Å, and 2.910 Å, respectively [CrO_2 COD database code: 1516110]. The Cr_2O_3 phase possesses a $R\bar{3}c$ structure, and its standard cell lattice parameters, represented by the lengths a, b, and c, are 4.9607 Å, 4.9607 Å, and 13.599 Å respectively [Cr_2O_3 COD database code: 9008084]. In this setup we could detect CrO_2, Cr_2O_3 and Quartz (sample holder) peaks. XRD data were fitted with two-phase as well as three phase model. The two-phase model contains CrO_2 and Cr_2O_3 phase, which is expected in these samples. However, the additional phase originated from the quartz glass cover-slip which is basically the sample holder signal. Including this phase led to significant improvement in the quality of the fit. During the three-phase refinement, we

observed small but clear peaks in certain regions of the XRD pattern. To avoid force-fitting and unphysical refined parameters, we initially excluded these regions. We considered the possibility that these peaks might be related to impurities like Cr_8O_{21}, Cr_2O_5 that could be present due to the high-pressure synthesis process [Ref. 35]. We weren't able to detect peaks of those impurities during refinement. We also introduced a preferred orientation parameter during the three-phase refinement. This parameter helped improve the chi-squared values, indicating better fitting of the data to the model.

Table 3.2 Comparison of χ^2 values for 2 phase and 3 phase refinement

T(K)		
	CrO_2, Cr_2O_3	CrO_2, Cr_2O_3, Quartz
50	2.78	1.98
100	2.94	2.05
150	2.89	2.07
200	2.96	2.06
230	2.77	1.96
235	3.01	1.99
240	2.94	2.18
245	2.98	1.91
250	3.54	2
256	2.94	2.02
260	3.07	1.91
266	3.05	2.08
280	2.74	1.95
298	3.19	2.16

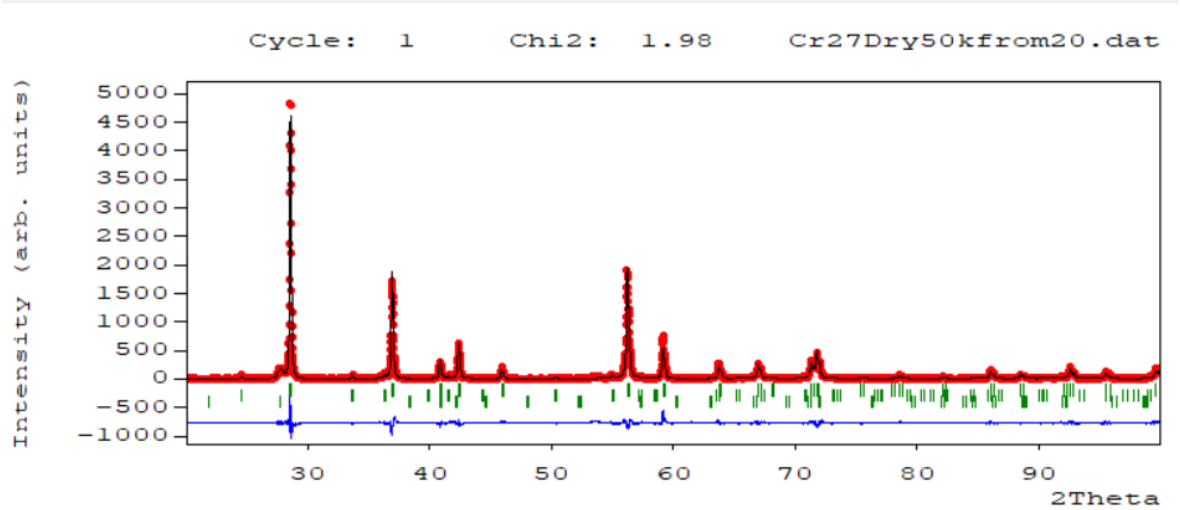

Fig 3.3 XRD and Rietveld Refinement at 50K for sample A3 for 3 phase

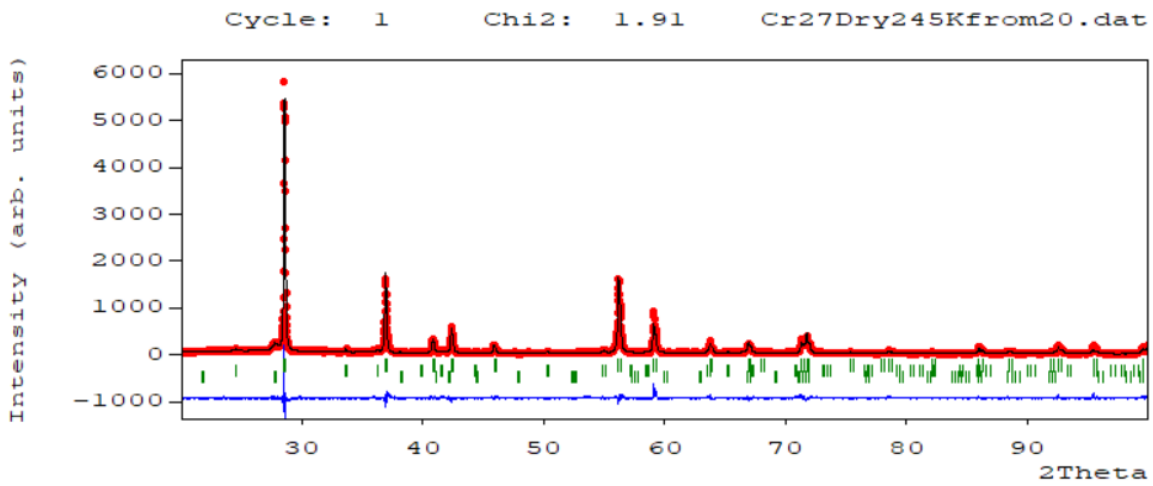

Fig 3.4 XRD and Rietveld Refinement at 245K for sample A3 for 3 phase

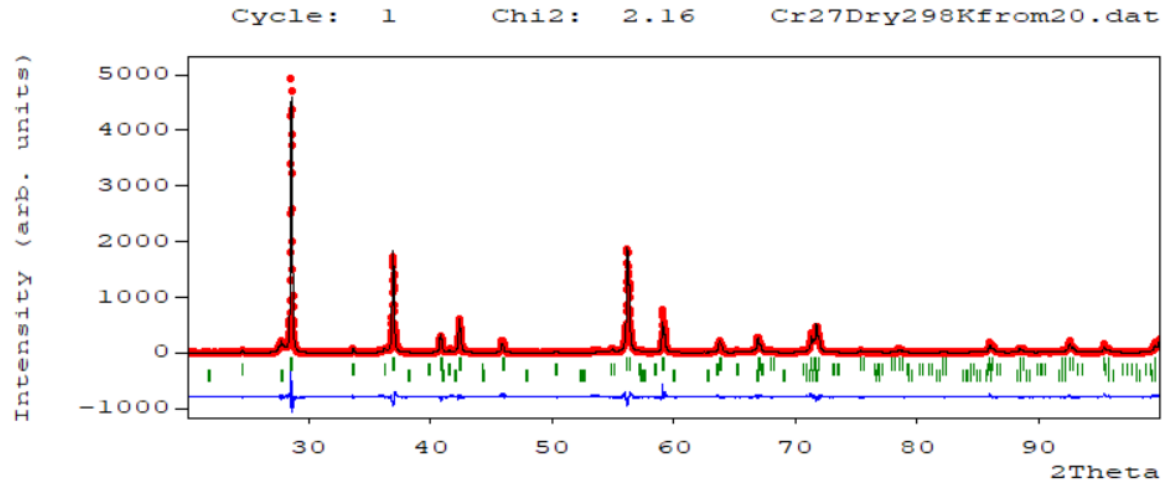

Fig 3.5 XRD and Rietveld Refinement at 298K for sample A3 for 3 phase

Figures 3.3, 3.4, 3.5 shows the results of Rietveld Refinement for 3 phases (CrO_2, Cr_2O_3 and Quartz). Here CrO_2 phase is fitted using $P4_2/mnm$ structure (CrO_2 COD database code: 1516110), Cr_2O_3 was fitted using $R\bar{3}c$ structure (Cr_2O_3 COD database code: 9008084) and Quartz was fitted using P 31 2 1 structure (Quartz COD database code: 9012601). Here the red dots are experimentally observed data and the black line is the fitted data.

3.4.1 Variation in cell parameters

In this section we compare temperature variation of lattice parameters, as obtained from 2 phase as well as 3 phase model discussed above.

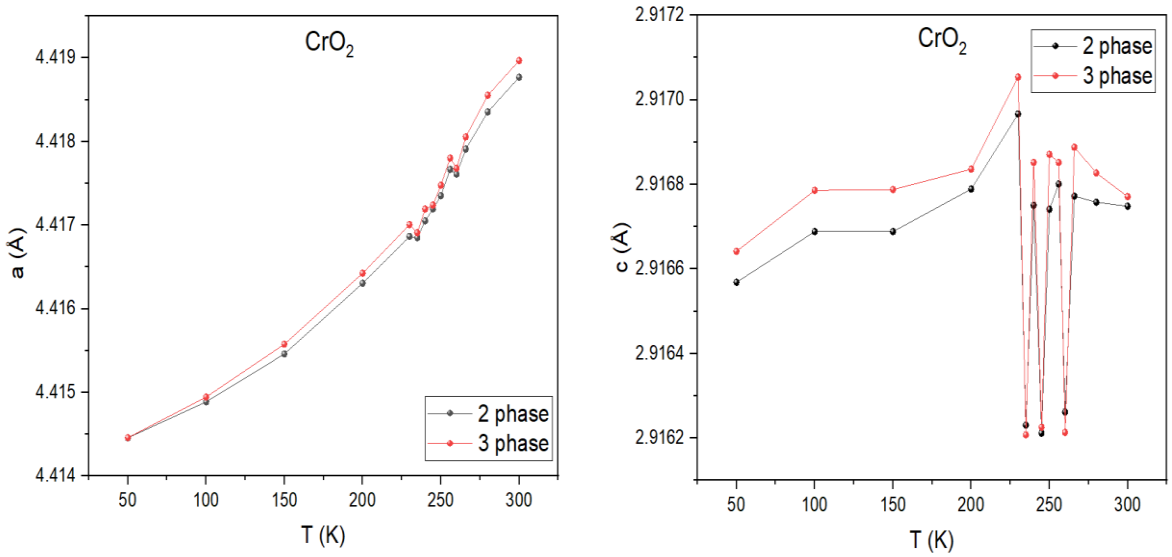

a b

Fig 3.6 a and b Temperature variation of lattice parameters for CrO_2 phase

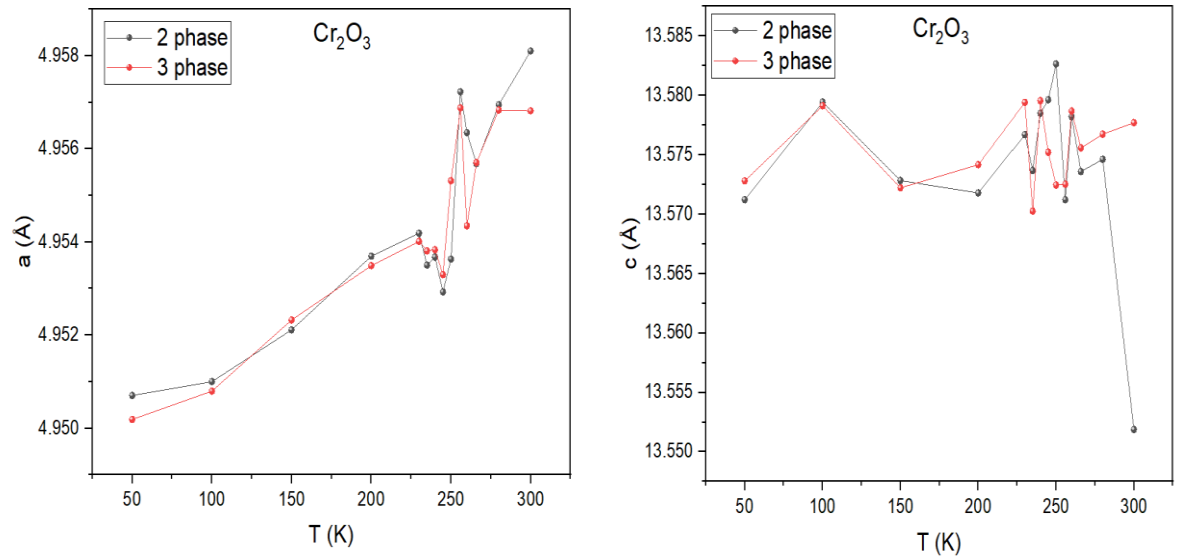

a b

Fig 3.7 a and b Temperature variation of lattice parameters for Cr_2O_3 phase

Observation and analysis:

The “a” and “c” lattice parameters of CrO_2 and Cr_2O_3 are plotted as a function of temperature. In case of CrO_2, the lattice parameter "a" increases with increase in temperature, which is expected. This trend is similar in case of 2 phase and 3 phase model. Lattice parameter “c” shows some anomaly above 200 K. These changes are seen in both 2 phase and 3 phase model. More data in this temperature range is needed to confirm these anomalies. The “a” parameter of Cr_2O_3, on the other hand shows a clear anomaly above 200 K. Here the lattice parameter reduces as a function of temperature and then increases again. For bulk Cr_2O_3, the ME transition is expected near 260K, where anomaly is seen the lattice parameter. However, in this case, Cr_2O_3 appears as ultra-thin layer. There is no structural or magnetic transition expected for CrO_2 in this temperature region. Hence the anomaly observed in lattice parameters of both CrO_2 and Cr_2O_3 appear to arise from strain at the interface. Temperature variation of lattice parameters of bulk Cr_2O_3 is needed to compare and associate this anomaly with magneto-electric transition.

To sum up, the examination of temperature-dependent lattice parameters highlights intriguing behaviours in both CrO_2 and Cr_2O_3. when it appears as a surface layer in CrO2. It is noteworthy that magnetoelectric effect in granular CrO_2 have been experimentally measured earlier. These enhanced magnetoelectric effects are attributed to interface effects [Ref 20] as CrO_2 is not a symmetry allowed magnetoelectric material but Cr_2O_3 is a known magnetoelectric. Further exploration, particularly with complementary data in the crucial temperature range, will contribute to a deeper understanding of these anomalies and their significance, especially concerning the magneto-electric transition in Cr_2O_3. The subsequent chapter delves into the analysis of specific heat data conducted on CrO_2.

Chapter 4

Specific Heat

Specific heat, a fundamental thermodynamic property, plays a pivotal role in our understanding of heat transfer and energy exchange in materials and systems. This extensive property quantifies the amount of thermal energy required to raise the temperature of a substance by a unit degree, and as such, it has profound implications across various scientific disciplines and practical applications. The study of specific heat is not only integral to our comprehension of thermal processes but also indispensable in the design and optimization of diverse technologies, from efficient energy storage and conversion systems to the development of advanced materials. In this thesis, we delve into the multifaceted realm of specific heat, exploring its underlying principles, measurement methodologies, and its far-reaching implications in fields such as materials science, engineering, and environmental science.

4.1 Low Temperature specific heat:

Low T Specific Heat:

$$C = C_{electron} + C_{phonon} + C_{magnon}$$ [Ref. 28]

4.1.1 Debye Specific heat (Phonon contribution):

The Debye specific heat is a theoretical model used to describe the heat capacity of a solid as a function of temperature. It was developed by Peter Debye in the early 20th century and is based on the idea of treating the vibrational modes of a solid as quantized phonons, similar to the way Einstein-Bose statistics are applied to particles.

$$U = \frac{9N_A K_B T^4}{T_D^3} \int_0^{\frac{T_D}{T}} \frac{x^3}{e^x - 1} dx$$

where,

T_D is Debye Temperature

In the low temperature limit

$$C_V = \frac{12\,\pi^4 N_A K_B}{5T_D^3} T^3$$

4.1.2 Electron contribution to specific heat:

In a metal, the electrons responsible for electrical conduction are close to the Fermi level, which is the highest energy level that electrons can occupy at absolute zero temperature. This region of electron energy levels near the Fermi level is referred to as the "Fermi Sea." These electrons are often depicted as if they form a sea of electron states, with the Fermi level being the surface of this

Using Fermi-Dirac statistics, only a small fraction of the electrons is available to participate in specific heat. This fraction contributes a specific heat and is only relevant at very low temperatures

$$C_V = \frac{\pi^2 N_A K_B^2}{2E_F} T$$

4.1.3 Magnon contribution to specific heat:

The approach for determining the magnon contribution to the specific heat of a magnetic solid closely resembles the widely recognized method used to calculate the phonon contribution to the specific heat in non-magnetic solids.

$$U_{magnon} = \frac{K_B T}{4\pi^2} \left(\frac{K_B T}{D_{stiff}}\right)^{3/2} \int_0^{x_m} \frac{x^{3/2}}{e^x - 1}\, dx$$

Where, $x = \frac{\Delta + D_{stiff} k^2}{K_B T}$

Since specific heat is obtained by temperature derivative for long spin waves:

$$C_{magnon} = \frac{K_B}{4\pi^2} \left(\frac{K_B T}{D_{stiff}}\right)^{3/2} \int_0^{\infty} \frac{x^{5/2}}{(e^x - 1)^2}\, dx$$

$$C = \gamma T + \beta T^3 + \alpha T^{\frac{3}{2}} \qquad (1)\ \text{[Ref. 28]}$$

4.2 Low Temperature Specific Heat measurement:

Specific Heat measurement is done on Physical property measurement system (PPMS) of prof A.K Nigam lab in TIFR Mumbai. Specific heat data is recorded from 2 K to 300 K and curve fitting is done below 15K.

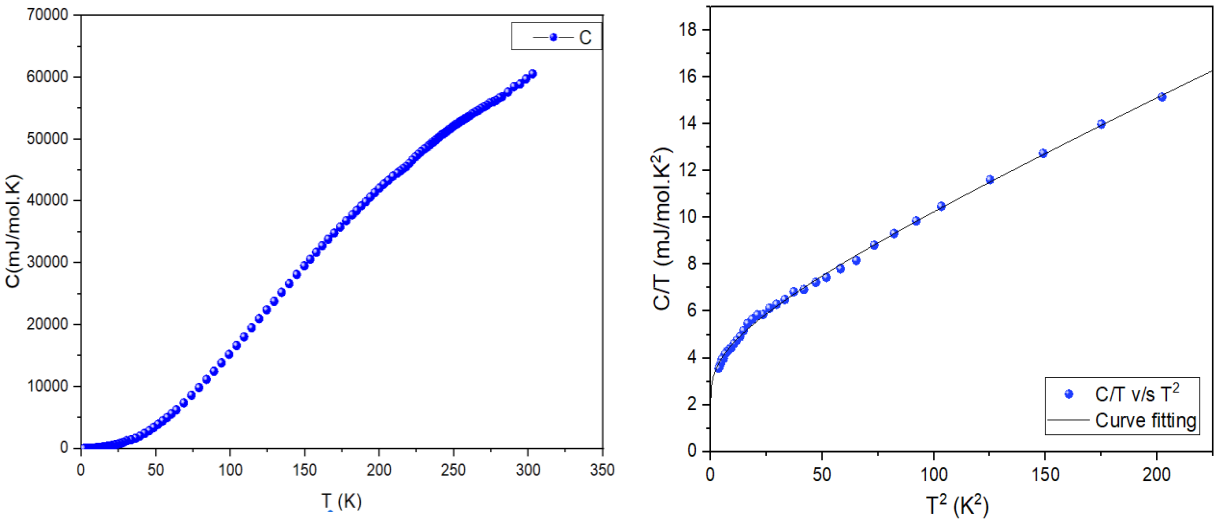

a b

Fig 4.1 Specific Heat data recorded on PPMS setup a) C v/s T data recorded in the range 2K to 300K, b) C/T v/s T^2 where solid line is fit to Eq.(1)

Table 4.1 Calculated specific heat contributions and constants

Parameters	Units	Measured	Std Error	For Coey
γ	$mJ/molK^2$	1.605	0.231	5.1
β	$mJ/molK^4$	0.04	0.001	0.028
α	$mJ/molK^{5/2}$	1.469	0.109	1.9

Calculated	Units	Our sample	Coey
D.O.S at Fermi Level	states/eV	0.681	2.2
Debye Temperature	K	365	593

We can clearly observe that our D.O.S at Fermi level calculation matches very closely with theoretical value of 0.69 states/eV [Ref. 28]. The calculated Debye Temperature for our sample is 365K.

Chapter 5

Transport measurements

Electrical and magnetic transport measurements are essential tools in understanding the behavior of materials, but they are subject to a myriad of influencing factors. One critical consideration is the sample size, as it can introduce quantum effects in smaller samples, leading to distinct electrical or magnetic behavior, while larger samples may present different conductive or magnetic properties. Additionally, the sample's shape plays a pivotal role, with thin films and nanoparticles often displaying unique characteristics compared to bulk materials. The sample's morphology, defects, grain boundaries, and crystallographic orientation can significantly influence transport properties. Materials that exhibit anisotropic behavior introduce another layer of complexity, where properties vary depending on the measurement direction,

For sample such as granular CrO_2, in which the grain is ferromagnetic and the surface layer of each grain is antiferromagnetic and magnetoelectric, the electrical transport is likely to be influenced by magnetic field, electric field as well as temperature. The large magnetoresistance and magnetoelectric effect has been measured in these samples [Ref 17]. In this chapter we present electrical transport in granular CrO_2 with different morphology, such as shown in the SEM data presented in chapter 3. Here, we have explored R vs T in different magnetic field. In addition, we have also measured R vs T using different bias current and observed significant electro resistance.

5.1 Linkam:

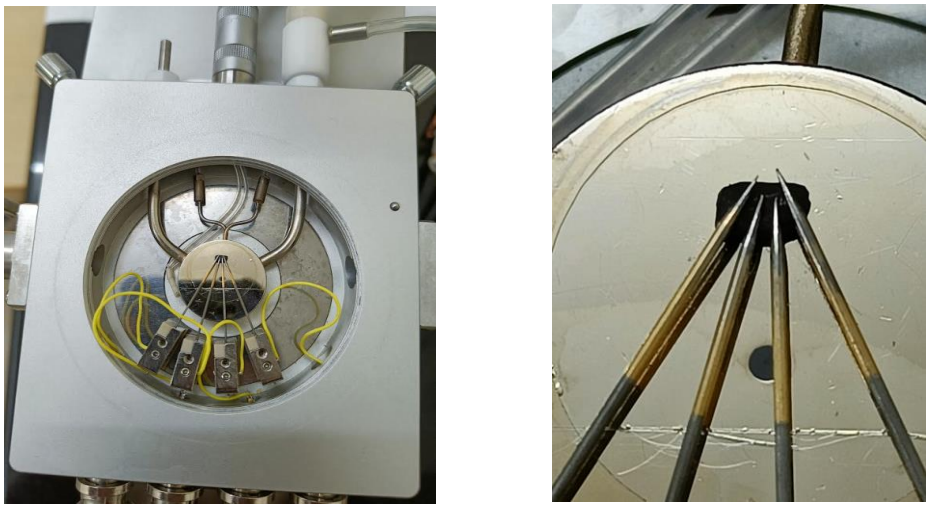

A B

Fig. 5.1 A and B. Four Probe connections on the Linkam stage

5.1.1 Low temperature measurement:

a) A2:

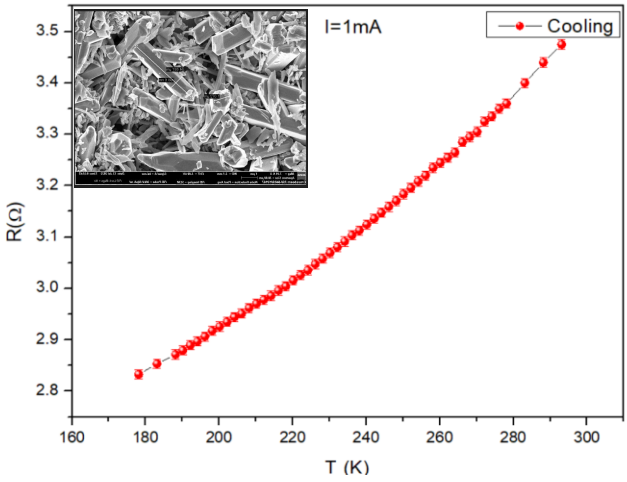

Fig 5.2 Electrical transport Measurement for cooling run done on Linkam

This sample exhibited an unexpected metallic response during a four-probe measurement conducted on a Linkam stage. This behaviour was observed even during the second measurement run. Typically, metallic behaviour is associated with transport measurements of thin film CrO_2, but this marks the first instance of such behaviour being observed in a bulk sample during transport measurements.

Since metallic behaviour is not typically observed in granular CrO_2, especially the R vs T data in needle-like commercial powders [Ref 26] as well as similar samples consisting of micron size rods of CrO_2 [Ref 17], it was surprising to see metallic region in wide temperature range of 180 K to 300 K as shown in Fig 5.2. Since this measurement involves adjusting 4 metallic probes in constrained sample area of less than 2mm X 2mm, there is a possibility of probe shorting. Hence, we repeated this measurement and could still find signatures of metallic conductivity in sample A2. Since this sample contained inter-connected thin rods of CrO_2, in addition to micron size rods, the possibility of metallic contact between CrO_2 grain may also lead to observed metallic behaviour. At this point, the data on sample needs to be repeated using PPMS or CCR.

b) A3a:

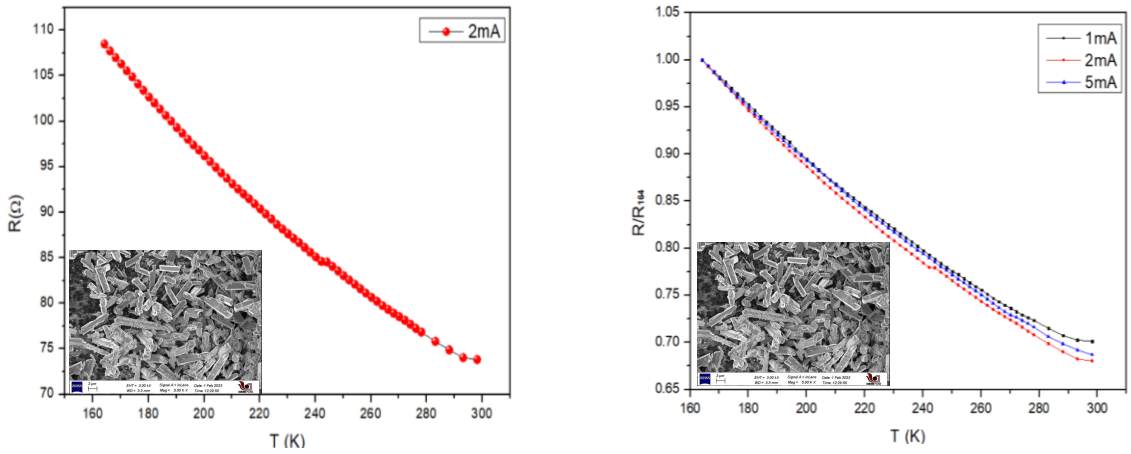

a b

Fig 5.3 Electrical Transport data was recorded for cooling cycle (300K to 164K)

a) R v/s T for 2mA current, b) R/R_{164} v/s T for different currents

In the electrical transport measurement for 2mA current, we can observe a slight change in slope around 241 K. This may be due to magnetoelectric transition of Cr_2O_3 surface layer phase. We also observed a correlation with current. Although we couldn't discern a significant alteration in the slope when applying 1mA and 5mA currents, the general trend in the graph remained similar across various current levels. It's important to highlight that, despite the metallic behaviour exhibited by thin CrO_2 films, sintered bulk sample demonstrates activated transport characteristics. This can be primarily attributed to the presence of an insulating Cr_2O_3 surface layer on each CrO_2 crystal within the sample.

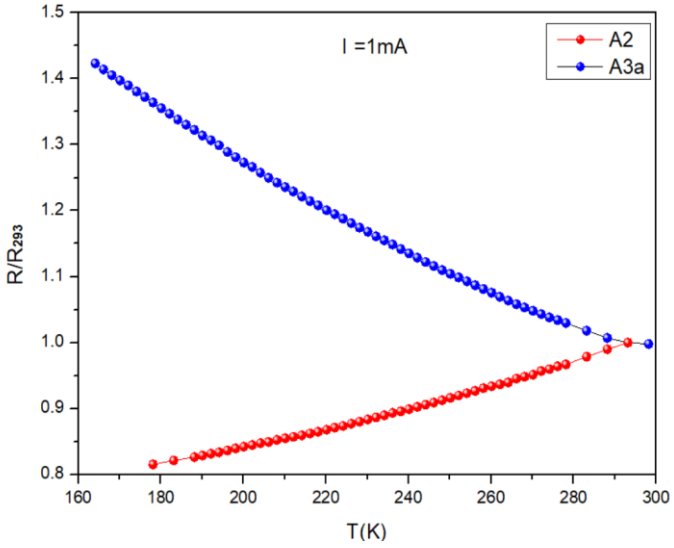

Fig 5.4 Comparison of R/R_{293K} for sample A2 and A3a

In fig 5.4 we clearly observe that change in sample morphology affects electron transport. Although both sample A2 and A3a contained micron sized crystals, sample A2 also contained very thin interconnected rods. Sample A3a showed activated transport behaviour while sample A2 showed metallic behaviour in temperature range of 180K to 293K.

Using linkam stage, we could not go below 160K due to experimental limitation. Hence, we repeated the same measurement using closed cycle refrigerator, down to 5K. Here one uses silver contact on the sample, rather than metallic needles, which are more appropriate for thin-film based devices that are larger in size. As shown in Figure 5.2, the electrical contacts are well separated from each other in a small pellet of granular CrO_2.

5.2 CCR:

5.2.1 Sample preparation:

- GE Varnish is used to stick CrO_2 pellet on sapphire.
- Four probe contacts were made on sample using scratched copper wires, silver conducting paste and Kapton tape
- Sapphire was stuck on gold plated copper holder of CCR using GE varnish
- Wires from the sample were then soldered to wires of CCR

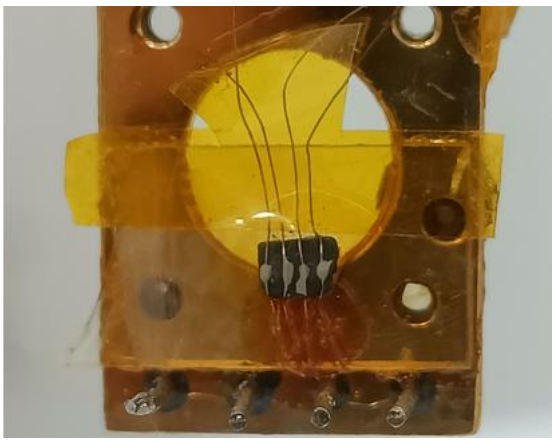

Fig 5.5 CCR sample holder connections

5.2.2 CCR measurements:

a) A2:

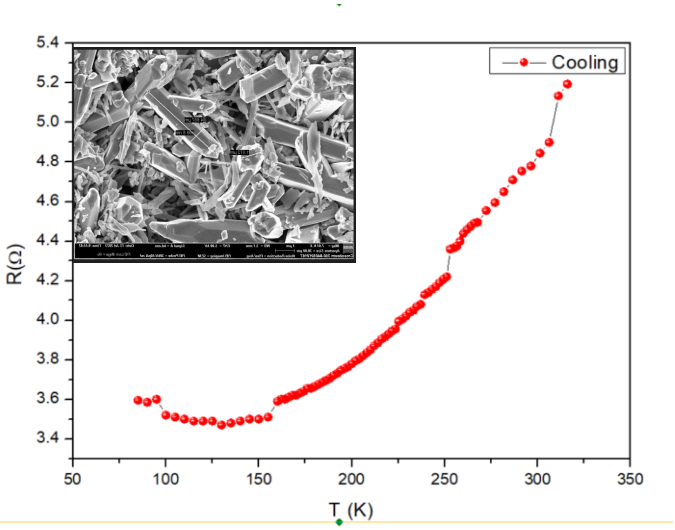

Fig 5.6 Electrical transport measurement on CCR

Below 150K, a tendency for activated region has been observed while above this temperature unexpected metallic behaviour was observed similar to Linkam measurements. Furthermore, we have observed a distinct change in slope occurring around 250K, which could be attributed to the magnetoelectric transition of the Cr_2O_3 surface layer. We did not have sample A2 in large quantity to further probe this particular sample. However, these data provided us motivation to perform R vs T in different bias current in other samples.

5.3 CFMS measurement:

For measuring R vs T in presence of magnetic field from room temperature down to 5K, we used CFMS facility in which magnetic field upto 7 Tesla can be applied, using a superconducting magnet. The measurements were performed on sample UNK.

Initial cooling and heating run with bias current of 1mA and no magnetic field was done on sample to observe remanence.

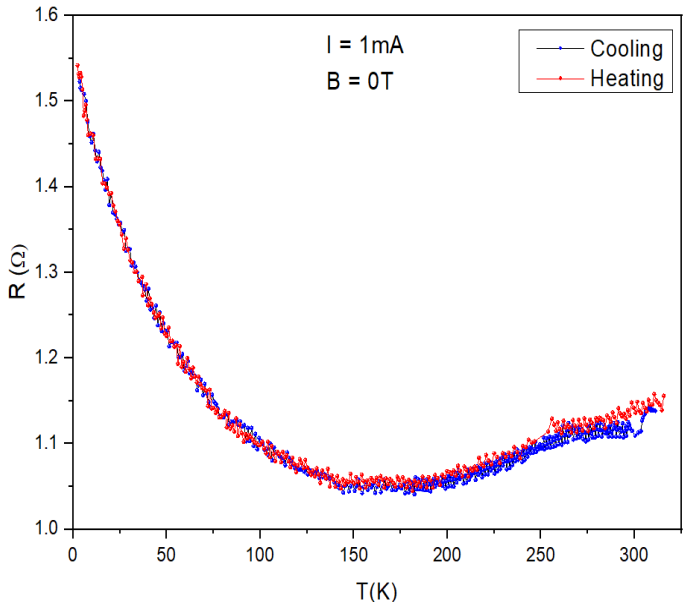

Fig 5.7 Cooling and heating curve

In fig 5.8, we first did cooling and then heating for fixed bias current 1m A and no external magnetic field. This sample showed activated transport upto 200K followed by metallic behaviour. Above 200 K, there was slight difference in heating - cooling cycle, which could not be better resolved, due to noise. However, a change of slope was detected above 250 K in both cycles.

I-V measurements were recorded at 3 different temperatures during cooling cycle

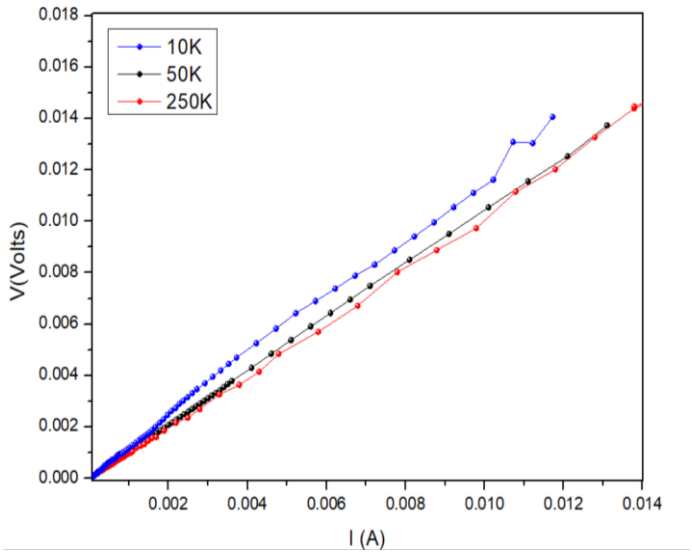

Fig 5.8 I-V at different temperatures

In fig 5.9, we observe that at 10K I-V curve isn't perfectly linear while at both 50K and 250K I-V curve is very linear

In the magnetotransport runs, magnetic fields of 1T and later 5T were applied under a bias current of 1mA. The data was compared with initial cooling run with no magnetic field and same bias current

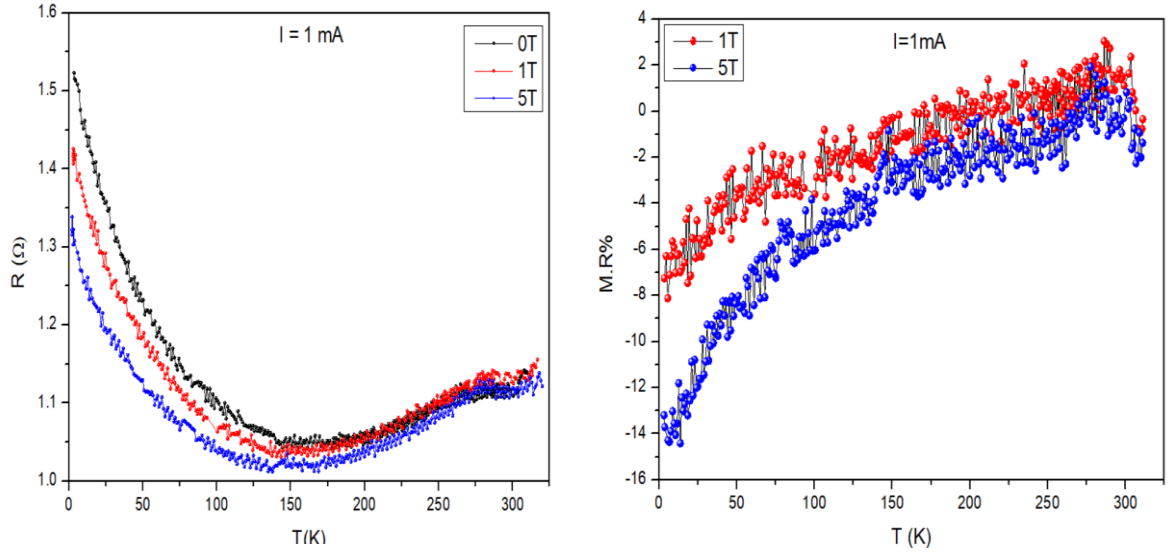

a b

Fig 5.10 Magnetoresistance measurement for cooling curves: a) R v/s T data, b) M.R% data

As shown in fig 5.11 b, we observe significant magnetoresistance in this sample. Value ranges from -1.5% at 298K to -7.24% at 3.4 K for 1T field. For 5T field, value ranges from -1% at 298K to -13.2% at 3K.

We observe 2 distinct regions. Below 150K we observe activated transport behaviour due to insulating grain boundary. Above 150K, we start observing an unexpected metal metallic behaviour with a change in slope in the region between 250K to 300K.

Electrotransport measurements were done after magnetotransport measurements. In the first electrotransport run 0.1m A and the next run 10m A bias current was used. Both these runs were compared with initial first cooling run (bias current 1m A).

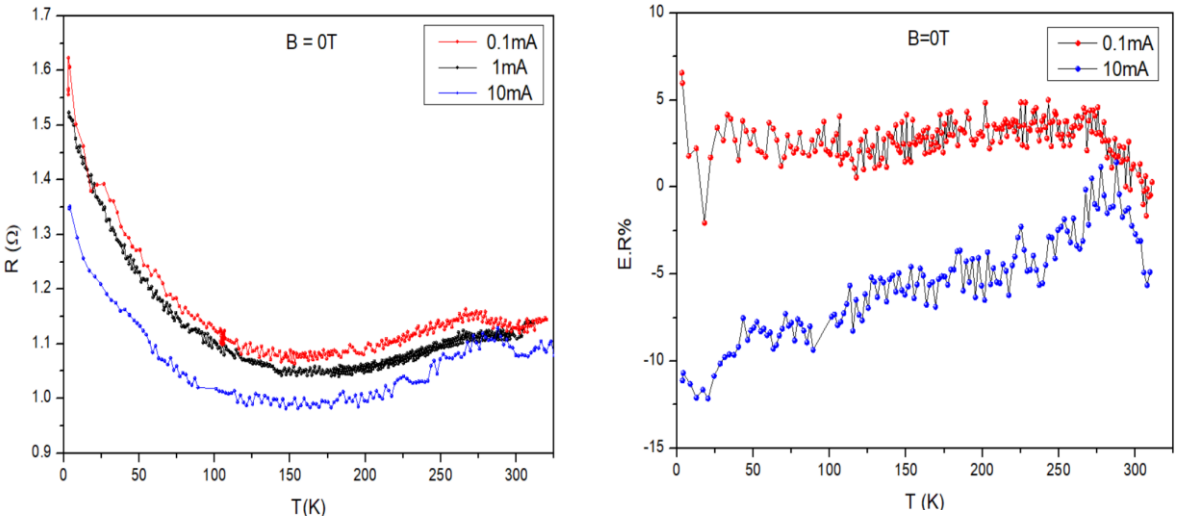

a b

Fig 5.9 Electroresistance measurement for cooling curves: a) R v/s T data, b) E.R% data

As shown in fig 5.10 b, we observe significant electroresistance in this sample. Value ranges from 1.06% at 298K to 6.6% at 3.3K for 0.1mA bias current. For 10mA bias current, value ranges from -2.2% at 298K to -11% at 3.8K.

We observe a significant current dependence (electroresistance) in the sample. Upto 150K, activated transport behaviour is observed. Above 150K, we observe metallic behaviour with a slope change in region between 250K and 300K.

Thus, in the electric and magnetic transport measurements on sample UNK, A2 two distinct regions are noticeable. As anticipated, the first region displays non-metallic behaviour, attributed to the presence of an insulating surface layer of Cr_2O_3. However, with increasing temperature we observe metallic behaviour similar to what is observed in thin film transport studies. Additionally, significant magnetoresistance and electro-resistance effects are also observed in sample UNK which are of comparable values. In sample A3a, activated transport behaviour was visible at higher temperatures also. These findings indicate that the bulk transport properties of CrO_2 are influenced by a combination of the magnetoelectric and insulating properties of Cr_2O_3 (nature of grain boundary) and morphology of sample.

Chapter 6

Conclusion

In conclusion, we have successfully conducted electric and magnetic transport measurements, as well as temperature-dependent Rietveld refinement of X-ray diffraction (XRD). The data analysis revealed valuable insights, particularly in understanding the magnetoelectric transition of the Cr_2O_3 surface layer and its potential impact on transport measurements.

In our study, we have discovered that the electrical transport properties of our samples depend on crystallite size and connectivity. Depending on the crystallite size and connectivity, our electron transport measurements reveal the presence of both an activated transport region and a metallic region within the material. This intriguing coexistence suggests complex electronic behaviour. Our findings extend beyond conventional expectations. We have observed not only a remarkably large tunneling magnetoresistance but also a notably significant electro-resistance in these samples. This combination of effects in our transport measurements is indicative of the multifunctional nature of the material's electrical behavior.

Hence, our research indicates that the electrical transport properties are influenced not only by the ultra-thin insulating surface layer of Cr_2O_3 but also by the magnetoelectric characteristics of Cr_2O_3. This dual influence highlights the intricate interplay of factors contributing to the transport properties, making our study an important contribution to the understanding of these materials.

6.1 Future prospect:

Our findings indicate presence of electroresistance which is as significant as magnetoresistance and hence this data needs to be repeated on different samples with the same morphology. In addition, it would be interesting to see if grains aligned in magnetic field lead to larger magnetoresistance in these samples.

Bibliography

1. J. P. Dismukes, D. F. Martin, L. Ekstrom, C. C. Wang, and M. D. Coutts (1971). Ferromagnetic Chromium Dioxide for Magnetic Tape. Product R&D 10 (3), 319-329. DOI: 10.1021/i360039a013
2. https://www.chemeurope.com/en/encyclopedia/Chromium%28IV%29_oxide.html.
3. https://tapetardis.wordpress.com/2012/05/15/the-type-ii-chrome-bias-audio-cassette/
4. The Materials Project. Materials Data on CrO_2 by Materials Project. United States. doi: https://doi.org/10.17188/1194001
5. The Materials Project. Materials Data on Cr_2O_3 by Materials Project. United States. doi: https://doi.org/10.17188/1194409
6. https://www.britannica.com/science/magnetism
7. P. Schlottmann. Double-exchange mechanism for CrO_2. PHYSICAL REVIEW B 67, 174419 (2003). DOI: 10.1103/PhysRevB.67.174419.
8. P. Schlottmann (2004). Double exchange and charge fluctuations in CrO_2. J. Appl. Phys. 95, 7471–7473. https://doi.org/10.1063/1.1667801
9. D. I. Khomskii, G. A. Sawatzky, M. A. Korotin and V. I. Anisimov (11 MAY 1998). CrO_2: A Self-Doped Double Exchange Ferromagnet. PHYSICAL REVIEW LETTERS. VOLUME 80, NUMBER 19.
10. Osmond, W. P. (1962). Indirect Magnetic Exchange Interactions in α-Fe2O3 and Cr2O3. Proceedings of the Physical Society, 79(2), 394–398. doi:10.1088/0370-1328/79/2/319.
11. Heather A. Bullen and Simon J. Garrett. Epitaxial Growth of CrO_2 Thin Films on TiO_2 (110) Surfaces. Chem. Mater. 2002, 14, 243-248.
12. Florian Thöle, Andriani Keliri , Nicola A. Spaldin (2020). Concepts from the linear magnetoelectric effect that might be useful for antiferromagnetic spintronics. *J. Appl. Phys.* 127, 213905. https://doi.org/10.1063/5.0006071
13. J. M. D. Coey and M. Venkatesan (2002). Half-metallic ferromagnetism: Example of CrO_2 (invited). American Institute of Physics. DOI: 10.1063/1.1447879
14. I. V. Solovyev, I. V. Kashin, and V. V. Mazurenko. Mechanisms and origins of half-metallic ferromagnetism in CrO_2. PHYSICAL REVIEW B 92, 144407 (2015). DOI: 10.1103/PhysRevB.92.144407.

15. Coey, J.M.D., Venkatesan, M., Bari, M.A. (2002). Half-Metallic Ferromagnets. In: Berthier, C., Lévy, L.P., Martinez, G. (eds) High Magnetic Fields. Lecture Notes in Physics, vol 595. Springer, Berlin, Heidelberg. https://doi.org/10.1007/3-540-45649-X_15.
16. Mukul S. Laad, L. Craco, and E. Mu¨ller-Hartmann. Orbital correlations in the ferromagnetic half-metal CrO_2. PHYSICAL REVIEW B, VOLUME 64, 214421. DOI: 10.1103/PhysRevB.64.214421.
17. A. Bajpai and A. K. Nigam (2007). Fluctuation-induced tunneling conductance and enhanced magnetoresistance in polycrystalline CrO_2 and its composites. PHYSICAL REVIEW B 75, 064403. DOI: 10.1103/PhysRevB.75.064403.
18. GHIMIRE, M. P., SANDEEP, & THAPA, R. K. (2010). STUDY OF THE ELECTRONIC PROPERTIES OF CrO_2 USING DENSITY FUNCTIONAL THEORY. Modern Physics Letters B, 24(20), 2187–2193. doi:10.1142/s0217984910024432
19. E. Yu. Beliayev , V. A. Horielyi, Yu. A. Kolesnichenko (2021). Magnetotransport properties of CrO_2 powder composites (Review article). *Low Temp. Phys.* 47, 355-377. https://doi.org/10.1063/10.0004228.
20. A. Bajpai, P. Borisov, S. Gorantla, R. Klingeler, J. Thomas, T. Gemming, W. Kleemann and B. Buchner (2010). Interface-driven magnetoelectric effects in granular CrO_2. EPL, 91 17006. DOI: 10.1209/0295-5075/91/17006.
21. A. Gupta; X. W. Li; Gang Xiao (2001). Inverse magnetoresistance in chromium-dioxide-based magnetic tunnel junctions. Appl. Phys. Lett. 78, 1894–1896. https://doi.org/10.1063/1.1356726
22. P. Das; A. Bajpai; Y. Ohno; ... et. al (2012). On the influence of nanometer-thin antiferromagnetic surface layer on ferromagnetic CrO_2. Journal of Applied Physics 112, 053921. https://doi.org/10.1063/1.4751350
23. Zheng, R. K., Liu, H., Wang, Y., & Zhang, X. X. (2004). Cr2O3 surface layer and exchange bias in an acicular CrO2 particle. Applied Physics Letters, 84(5), 702–704. doi:10.1063/1.1644919.
24. L. Ranno; A. Barry; J. M. D. Coey (1997). Production and magnetotransport properties of CrO_2 films. Journal of Applied Physics 81, 5774–5776. https://doi.org/10.1063/1.364682.
25. Jianbiao Dai and Jinke Tang. Junction-like magnetoresistance of intergranular tunneling in field-aligned chromium dioxide powders. PHYSICAL REVIEW B, VOLUME 63, 054434. DOI: 10.1103/PhysRevB.63.054434

26. A. Barry, J. M. D. Coey, A. E. Berkowitz, Ll. Balcells, and F. F. Putris (27 APRIL 1998). Magnetoresistance of Chromium Dioxide Powder Compacts. PHYSICAL REVIEW LETTERS VOLUME 80, NUMBER 17.
27. A. Barry, J. M. D. Coey, S. M. Watts, S. Wirth, and S. von Molna´r (1 APRIL 2000-II). Evidence for two-band magnetotransport in half-metallic chromium dioxide. PHYSICAL REVIEW B VOLUME 61, NUMBER 14.
28. A. Barry; J. M. D. Coey; L. Ranno; ... et. al (1998). Evidence for a gap in the excitation spectrum of CrO_2. Journal of Applied Physics 83, 7166–7168. https://doi.org/10.1063/1.367791.
29. Ping Sheng. Fluctuation-induced tunneling conduction in disordered materials. PHYSICAL REVIEW B VOLUME 21, NUMBER 6 (15 MARCH 1980).
30. E. Yu. Beliayev, V. A. Horielyi, Yu. A. Kolesnichenko (2021). Magnetotransport properties of CrO_2 powder composites (Review article). Low Temperature Physics 47, 355–377. https://doi.org/10.1063/10.0004228.
31. T Yu, Z X Shen, W X Sun, J Y Lin and J Ding (2003). Spin–phonon coupling in rod-shaped half-metallic CrO_2 ultrafine particles: a magnetic Raman scattering study. J. Phys.: Condens. Matter 15 L213–L217.
32. V. S. Oudovenko, S. Y. Savrasov, A. Toropova and G. Kotliar (2005). Electronic structure and magnetic anisotropy of CrO_2. PHYSICAL REVIEW B 71, 172403. DOI: 10.1103/PhysRevB.71.172403.
33. B. L. Chamberland (1977). The chemical and physical properties of CrO_2 and tetravalent chromium oxide derivatives, Critical Reviews in Solid State and Materials Sciences, 7:1, 1-3. DOI: 10.1080/10408437708243431.
34. L. Ranno, A. Barry, and J. M. D. Coey (1997). Production and magnetotransport properties of CrO_2 films. J. Appl. Phys. 81, 5774. DOI: 10.1063/1.364682
35. A. Bajpai and A. K. Nigam (2005). Synthesis of high-purity samples of CrO_2 by a simple route. Applied Physics Letters 87, 222502. DOI: 10.1063/1.2136411.
36. KUBOTA, B. (1961). Decomposition of Higher Oxides of Chromium Under Various Pressures of Oxygen. Journal of the American Ceramic Society, 44(5), 239–248. doi:10.1111/j.1151-2916.1961.tb15368.x.
37. C.W. Oatley, W.C. Nixon, and R.F.W. Pease (1965). Scanning electron microscopy. Advances in Electronics and Electronic Physics, 21:181
38. https://microscopewiki.com/scanning-electron-microscope/
39. H.P. Klug and L.E. Alexander (1974). X-Ray Diffraction Procedures: For Polycrystalline and Amorphous Materials. John Wiley and Sons 2nd Edition.

40. https://pubs.usgs.gov/of/2001/of01-041/htmldocs/xrpd.htm
41. R.A. Young (1993). The Rietveld Method. International Union of Crystallography. Oxford University Press.
42. https://www.linkam.co.uk/electricalapplications
43. https://qd-europe.com/at/en/product/physical-property-measurement-system-ppms/
44. https://www.arscryo.com/closed-cycle-cryocoolers
45. http://www.cryogenic.co.uk/products/mini-cryogen-free-systems-mcfms-3-7-tesla
46. Charles Kittel. Introduction to Solid State Physics, 8th edition
47. Stephen Blundell (2001). Magnetism in Condensed Matter. Oxford University Press.
48. http://hyperphysics.phy-astr.gsu.edu/hbase/thermo/Debye.html#c2
49. Rohlf, James William (1994). Modern Physics from a to Z. Wiley.
50. Schroeder, Daniel V (2000). An Introduction to Thermal Physics. Addison-Wesley.